LUND UNIVERSITY
Faculty of Science

Linköping University
FACULTY OF HEALTH SCIENCES

Quantitative tissue classification with dual-energy computed tomography for radiation treatment planning: evaluation and optimization of a new method

Mattias Karlsson

Master of Science Thesis in
Medical Radiation Physics

Linköping, December 2010

Supervisors: Alexandr Malusek, Gudrun Alm Carlsson, Michael Ljungberg

Jag ska göra några sista kalkyler
och studera förloppet i ett experiment
om förändringarna stöder teorin
så kan vatten förvandlas till vin

Kjell Höglund - Genesarets sjö

Abstract

A new method to extract mass density and elemental compositions of tissues from dual-energy computed tomography (DECT) scans is described and investigated. The method decomposes a tissue into proportions of two or three predefined base materials and was proposed in 2008 by a research team at Linköping University. Informations of tissue parameters may be important in radiation treatment planning to calculate the distribution of absorbed dose in the patient.

The study was performed with tissue compositions taken from scientific publications and the simulated response of a DECT scanner. The derived tissue parameters were used as input for Monte Carlo computer simulations of different types of radiation treatments to evaluate the effects on distributions of absorbed dose.

It was found that the accuracy of the extracted elemental compositions depended on the selected base materials. An inappropriate choice of base materials resulted in negative elemental weights, which are unphysical. Skeletal tissues were decomposed into proportions of cortical bone, yellow bone marrow and red bone marrow. 12 of 19 investigated skeletal tissues could be decomposed into positive elemental weights with the largest error of 3.0 percentage points. Properties for soft tissues were more difficult to determine with only one set of base materials. 29 of 51 soft tissues resulted in positive elemental weights when decomposed into proportions of water, lipid and protein. Errors up to 19.2 percentage points were seen in the elemental weights of the soft tissues. The simulated absorbed dose distributions of ^{192}Ir brachytherapy did not show any substantial dependence on different tissue compositions. The results from simulations with the lower energy photons emitted by ^{125}I were more affected by variations in tissue compositions. In both proton and ^{12}C-ion therapy simulations, the error in Bragg peak position introduced by the extracted tissue compositions were less than 0.3 mm.

This study indicates that an appropriate choice of base materials is crucial in order to determine accurate tissue compositions. The Monte Carlo simulations showed that elemental compositions may be important to consider in radiation treatment planning, especially for low-energy brachytherapy. Further evaluation with real DECT data is needed to see how the performance of the method is affected by for example image artifacts and individual variations in tissue compositions.

Author: Mattias Karlsson

Title: Quantitative tissue classification with dual-energy computed tomography for radiation treatment planning: evaluation and optimization of a new method

Master of Science Thesis in Medical Radiation Physics, 30 credits

Department of Medical Radiation Physics, Lund University

Contents

1 Introduction

Computed tomography (CT) is a medical imaging method that is capable of rapidly scan a patient to produce images of high spatial resolution and low geometrical distortion [1]. CT scanners are commonly used in medicine to provide anatomical images for diagnostics and staging of malignant diseases. In addition, the scanners are capable of obtaining quantitative information about the scanned patient [2].

The CT image can be considered as a spatial distribution of linear attenuation coefficients, $\mu(E)$ [2]. The CT-image represent the μ-values as CT numbers, N_{CT}, to decrease the dependence on the energy spectrum used.

Conventional CT scanners are equipped with an X-ray tube and a detector that rotates around the patient. Recent developments have made dual-energy CT (DECT) technique available, where an object is scanned with two different energy spectra. The extra projection data that is obtained in a DECT scan can potentially increase the possibilities to characterize and decompose the scanned tissue. Differences between the measurements of the two energy spectra can be used to draw conclusions of the scanned material.

The possibility to use CT scans with different energy spectra for material characterization was investigated already in the 1970s [3, 4]. However, insufficient technical performance of the early CT scanners hampered clinical implementation of dual-energy techniques [5]. Today dual-energy CT has gained new interest and several manufacturers provide the technique. Even though the technical solutions differ between manufacturers, they have the mutual aim to acquire CT data at two different X-ray energy spectra.

Quantitative information from CT scans are commonly used when planning radiation treatment [1] to evaluate different strategies, the resulting distributions of absorbed dose can be calculated with advanced computer software called treatment planning system. The result of the dose calculation depends, among other things, on the accuracy of the patient tissue data [6].

X-ray tube voltages used for diagnostic CT (approximately 60-140 kilovolt, kV) produce photon energy spectra for which the dominating interaction process is incoherent scattering. The cross-section for incoherent scattering is proportional to the electron density, ρ_e, of the absorbing medium [6]. As long as incoherent scatter dominates it is possible to set-up a relationship between N_{CT} and ρ_e [7]. This conversion from N_{CT} to ρ_e is of important for absorbed dose calculations in megavoltage (MV) X-ray therapy, where the predominate interaction is incoherent scatter as well [1].

Absorbed dose deposition characteristics for other types of radiation used for therapy may have larger dependences on the atomic number of than MV X-rays. For instance, therapy with heavy charged particles or brachytherapy with low-energetic photons have a substantially larger dependence on the atomic number, Z. A method capable to extract elemental compositions may improve these kinds of radiation treatments [8, 9].

1.1 Aim

The aim of the work presented in this thesis is to evaluate a three-material decomposition method based on DECT data. The method is applied in a computer study to extract elemental compositions of a wide range of tissues. Soft tissues are treated as a weighted mixture of water, lipid and protein, and skeletal tissues as a mixture of red bone marrow, yellow bone marrow and cortical bone.

Finally, the extracted tissue compositions influence to absorbed dose is evaluated in simulations of different types of radiation treatments, based on Monte Carlo techniques.

2 Background

2.1 Classification algorithms

Since the invention of the CT scanner, a lot of work has been put into determine tissue parameters from CT data. The motivation has mainly been diagnostic purposes, as to characterize urinary calculi [10] or to virtually subtract iodine contrast media from CT images [11, 10, 5]. Here follows a brief background to different approaches to classify and decompose tissues with CT.

The traditional classification method with single energy CT is threshold segmentation [12]. This is done by relating different intervals of CT numbers to different tissue types. The lowest CT numbers may be set to lung tissue with a certain composition and the highest numbers to compact bone. The elemental composition is fixed within each interval, while the mass density may be fitted to match the measured CT number. Figure 1 shows a simple example of a calibration curve for threshold classification. The calibration curve can be determined by scanning materials with known elemental compositions and density.

A drawback of the threshold segmentation method is that materials of different compositions may be associated with the same CT number, depending on the X-ray spectrum. In addition, it may be questionable how many tissue bins that should be used and where the boundaries between them should be set. Schneider et al. has shown that the phantom materials used influence the resulting calibration curve [13]. Verhagen and Devic found that misassiged tissues in threshold segmentation can lead to errors in absorbed dose up to 40% for 250 kV X-ray therapy [14].

Schneider, Bortfield and Schlegel proposed in 2000 a method to determine elemental compositions and mass densities by dividing the CT number scale into intervals and interpolate elemental weights and mass densities in each such interval [15]. The interpolation was done between the tissues confining the certain CT number region, so that each scanned tissue was interpreted as a mixture of the two boundary tissues. The authors extracted elemental compositions and mass densities for skeletal tissues with the base materials bone marrow (1:1 mixture of red and yellow) and cortical bone. Soft tissues were more difficult to decompose into proportions of only two base materials. These were proposed to be composed of mainly three materials; water, lipid and protein. The authors also investigated

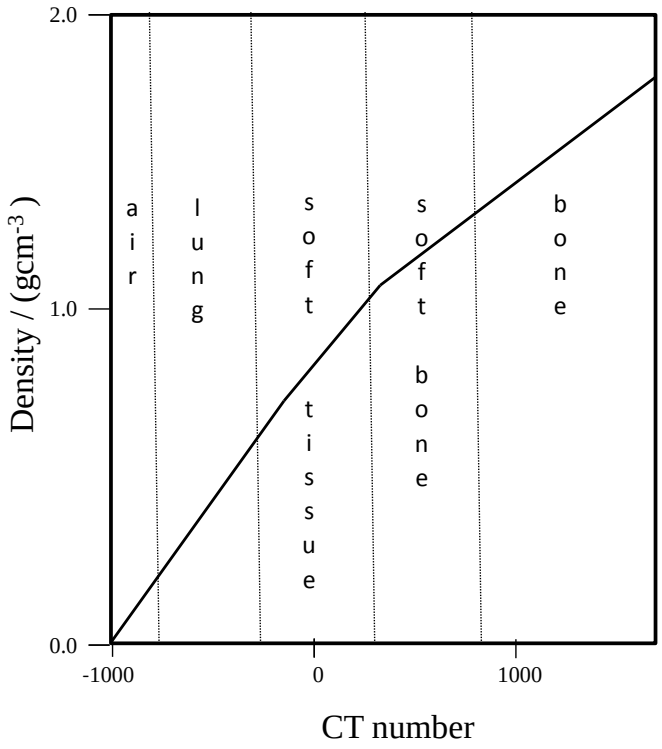

Figure 1: Example of threshold segmentation of the CT number scale to determine tissue properties. The elemental composition for a certain CT number is set according to the corresponding tissue type in the scale. Mass density is determined with the calibration curve. The thresholds are based on data from Bazalova et al. [12].

the possibilities to describe soft tissues with only two base materials, however resulting in relatively large errors.

In the 1970s, Alvarez and Macovski suggested a decomposition method using X-ray measurements at two different energies [4]. They expressed μ as a linear combination of two basis functions. The model was used to parametrize the total attenuation μ into contributions from photoelectric effect and incoherent scatter. The contribution from photoelectric effect was strongly dependent on the atomic number and the contribution from incoherent scatter on the electron density:

$$\mu(E) = K_1 \frac{\rho}{A} Z^n \frac{1}{E_3} + K_2 \frac{\rho}{A} f_{KN}(E) \tag{1}$$

where $\mu(E)$ is the linear attenuation coefficient of the medium at photon energy E, and ρ, A and Z are mass density, atomic weight and atomic number of the medium. K_1 and K_2 are constants that need to be determined by calibration. The parameter n represents the Z-dependence of photoelectric effect and is approximately equal to 4 at photon energies relevant for diagnostics [4].

The parametrization suggested by Alvarez and Macovski may provide effective Z and

effective ρ of a material. However, to perform Monte Carlo radiation treatment planning more detailed information about the elemental compositions is needed [15].

The method presented in this work uses an approach which can be considered as an extension to the method proposed by Schneider, Bortfeld and Schlegel [15]. The method expresses the linear (or mass) attenuation coefficient into contributions from different base materials, instead of interaction processes as proposed by Alvarez and Macovski. Similar base material approaches have recently been reported from other research teams, but the method has not yet been investigated for radiation treatment.

Clavijo et al. [11] used a base material method to visualize calcified plaque in vessels with iodinated blood. The method gave satisfying results with a monoenergetic X-ray beam and in absence of image artifacts. However, when using a polyenergetic beam hardening and scatter artifacts hampered successful material classification.

Liu et al. [16] investigated a three-material decomposition method in phantom studies to determine the concentrations of hydroxyapatite in mixtures of water, hydroxyapatite and iron nitrate. They concluded that the validity of the method relied on using base materials with large differences in X-ray attenuation. It was found that scatter degraded the accuracy of CT numbers and affected the results negatively.

2.2 Computed tomography

A conventional single energy CT scanner acquires X-ray projections in a large number of angles with an X-ray source and detector that rotates around the patient. The projection data is reconstructed with mathematical methods to form axial 2D images of the patient anatomy. The reconstructed images can be considered as maps over linear attenuation coefficients, which are presented as CT numbers [2]. CT numbers are measured in Hounsfield units and are defined as:

$$N_{CT} = \frac{\mu - \mu_w}{\mu_w} 1000 \tag{2}$$

where μ is the linear attenuation coefficient for the voxel of interest and μ_w is the linear attenuation coefficient of water at the same X-ray energy. Following from the definition, pure water has $N_{CT} = 0$ and dry air $N_{CT} = -1000$.

To optimize image quality and accuracy of extracted μ-values it is important to minimize any sources of image artifacts. Such artifacts include beam hardening, caused by the usage of polychromatic X-ray energy spectra. At the concerned energy range, the attenuation of photons increases with decreasing energy. When passing through a medium, the low-energy photons will be attenuated to a higher degree, shifting the mean energy towards higher values. This beam hardening effect causes characteristic streaks and cupping artifacts in CT images, which may lead to errors in the reconstructed CT numbers. Modern CT scanners are capable to perform simple corrections for beam hardening, by assuming water-equivalent tissues [17, 2].

Dual-energy computed tomography - DECT

Dual-energy CT is a technique that uses two different X-ray energy spectra to scan an object. Different manufacturers have developed different solutions to implement DECT. Early experiments with dual-energy CT were performed using two separate CT scans with different tube voltages [18]. However, the non-simultaneous acquisitions were susceptible for mismatches of the two data sets due to organ or patient movements between the scans.

Other approaches have focused on the detector system. Using only one scan, an energy resolving detector enables the extraction of two μ-values [19]. This DECT approach is used by CT scanners from Philips [20].

General Electrics has an alternative DECT approach, using rapidly switching the X-ray tube voltage during the scan [21].

Yet another approach is used by Siemens. At the University Hospital in Linköping, a Siemens Somatom Definition Flash dual-energy CT scanner is installed. This scanner is equipped with two separate X-ray tubes with corresponding detectors. The X-ray tubes are positioned with an offset of 95 degrees. A schematic image of the dual source solution is shown in Figure 2. The figure shows that the 140 kV spectrum can be used with a so called selective photon shield, indicating 0.4 mm extra tin filtration. This filter blocks low-energy components from the high-energy spectrum, which helps to keep the absorbed dose to the patient low.

A possible drawback to the dual source solution compared to fast kV-switching and energy resolving detectors is a higher detection of scattered radiation. Photons from the one X-ray tube may be scattered and registered in the other detector system, and the other way around [22].

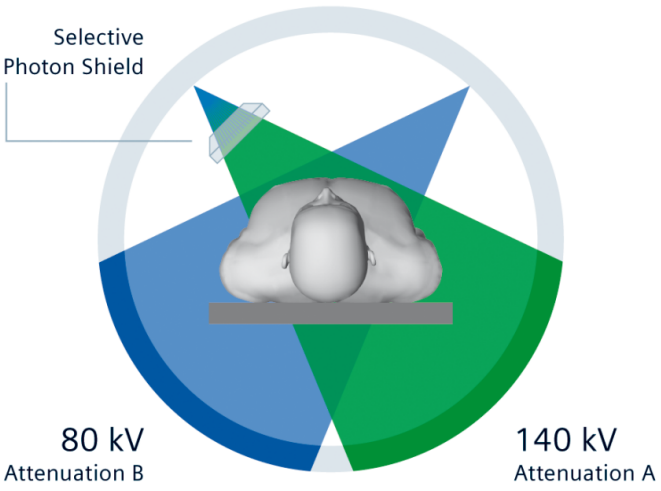

Figure 2: Schematic image of dual source CT principle. Image courtesy of Siemens.

2.3 Radiation treatment

Since the first reported treatments in the late 1890's [23], radiation treatment is today established as a reliable method for both palliative and curative treatment of cancer [6]. Several different approaches for radiation treatment have been developed, using different types of radiation and delivery techniques, each with their own advantages and drawbacks.

2.3.1 Treatment planning and interaction of radiation with matter

Treatment planning is the process of radiation therapy that concerns preparation and optimization of the treatment to achieve the prescribed absorbed dose.

CT data are commonly used in the radiation treatment planning process to delineate patient contours, target volumes and organs at risk, as well as providing μ-values to the treatment planning system (TPS) [6, 1]. The TPS calculates the distributions of absorbed dose which makes it possible to evaluate and compare different treatment strategies and optimize the treatment parameters. For these calculations to be accurate and realistic, the TPS needs to know how the radiation field will be modified in the tissue. Different types of radiation interact with tissue in different ways, mainly due to:

- the type of radiation (photons, electrons, protons, heavier ions etc.)
- the energy of the radiation
- the atomic composition and mass density of the absorbing medium

Properties of the clinical radiation beam is generally controlled and well known. But information of the patient tissues are generally not as well known and need to be extracted from e.g. CT scans.

The interactions of ionizing photons are described by the linear attenuation coefficient, μ, which represents the fraction of photons that will interact when traversing a unit path-length in a certain material. For energies relevant in medical applications, the possible interaction processes are photoelectric effect, pair production, coherent and incoherent scatter. The mass attenuation coefficient is produced by dividing μ with the mass density, ρ. Hence, this term is independent of the mass density and the state of aggregation of the material.

2.3.2 Brachytherapy

Brachytherapy concerns radiation therapy with the source positioned inside or close to the target volume. The sources used in brachytherapy generally emit photons and electrons with lower energies than those used in external beam therapy. This allows a more conformal distribution of absorbed dose and makes it easier to spare normal tissue, although it requires the tumor to be well localized [6].

Brachytherapy can be divided into temporary and permanent therapy. Permanent brachytherapy concerns implantation of radioactive sources into the target volume. The

sources are placed at positions calculated by the treatment planning system to achieve the prescribed absorbed dose. The sources are left in the tissue to continuously emit radiation that ideally kills the cancerous tissue. Prostate cancer is commonly treated with this technique, using the isotope ^{125}I [6].

Temporary brachytherapy can be performed with a high dose-rate source, of e.g. ^{192}Ir, which is generally assembled in a remotely controlled afterloader unit. The source is mounted on a wire and enters the target volume through inserted applicators. High dose rate is commonly given as a boost to external beam therapy of prostate cancer [24].

Treatment planning systems used today for brachytherapy are commonly based on the dosimetry formalism suggested by the Task Group-43 [25, 26] of the American Association of Physicists in Medicine (AAPM). The TG-43 formalism utilizes absorbed dose distributions around brachytherapy sources in water. For relatively low photon energies, as those emitted by ^{125}I ($E_{effective}$ approximately 28 keV) and ^{103}Pd ($E_{effective}$ approximately 21 keV), the use of water as reference medium may be questionable and may affect the resulting absorbed dose distribution, especially in the presence of high-Z heterogeneities, as tissue calcifications [27].

2.3.3 Therapy with protons and heavier charged particles

Protons and heavier charged particles have properties that make them advantageous to use for radiation treatment [28, 29].

The energy deposition increases with the depth in the medium, ending in a region of high energy deposition; the so called Bragg peak. Distal to the peak, the absorbed dose is zero for protons and negligible or relatively low for heavier charged particles.

Charged particles heavier than protons have the advantage of a higher biological effectiveness. This means that a lower absorbed dose is needed to achieve a certain biological effect. Particles heavier than protons have an even sharper Bragg peak, but have higher cross-sections for nuclear interactions, which produce a build-up of secondary particles along the beam path. The secondary particles generally have lower masses than the primary particles and will therefore have a longer range, giving a tail to the depth-dose that stretches past the Bragg peak [30].

In order to calculate the absorbed dose distribution prior to radiation therapy, it is necessary to know how the particle beam will be modified in the patient. In therapy with heavy charged particles, the quantity that needs to be determined is the stopping power, S. Stopping power is defined as the average energy loss per unit length for a charged particle traversing a medium. X-ray CT scanners are used to obtain a map of CT numbers, which are converted to stopping power values or to water-equivalent densities via calibration curves or look-up tables [31].

2.3.4 Monte Carlo treatment planning

Monte Carlo methods are widely recognized as the most accurate dose calculation techniques available today [32]. These methods simulate the track of every particle through a

defined geometry. Interactions and energy depositions are sampled from probability distributions with a random number generator. Monte Carlo systems for dose calculations generally requires that all materials present in the simulation geometry are specified with elemental compositions and mass densities. The accuracy of the dose calculation will depend on the quality of these tissue parameters.

Today, the use of these calculation models is restricted by computer power limitations. Developments in computer performance and the use of different variance reduction techniques may enable treatment planning based on Monte Carlo methods in clinical practice in the near future [32].

2.3.5 Stoichiometric calibration

Schneider et al. proposed in 1996 the stoichiometric calibration method to relate CT numbers to electron densities (for MV photon therapy) or stopping power (for proton therapy) [13]. This calibration method is today commonly used in proton therapy facilities [31, 33].

The stoichiometric calibration utilizes that μ for a mixture of elements, at a certain X-ray energy, can be written as:

$$\mu = \rho \mathrm{N}_A \sum_{i=1}^{N} w_i \frac{Z_i}{M_i} (\sigma_i^{ph} + \sigma_i^{inc} + \sigma_i^{coh}) \tag{3}$$

where ρ is the mass density, $\mathrm{N_A}$ is the Avogadro constant, M_i is the molar mass and w_i is the mass fraction of element i in the mixture. The terms σ^{ph}, σ^{inc} and σ^{coh} are the atomic cross-sections for photoelectric effect, incoherent and coherent scatter at the considered X-ray energy and element.

When using phantom materials with known properties, Eq. 3 together with tabulated cross-section values could be used to relate CT numbers to electron density (or stopping power). However, the energy spectrum used by CT scanners is often not exactly known, nor is the detection efficiency of the detector system. Instead the stoichiometric calibration method uses a parametrization of the cross-sections. The total atomic cross-section for element i can be described by:

$$\sigma_i^{tot} = \sigma_i^{ph} + \sigma_i^{coh} + \sigma_i^{inc} = K^{ph}(E) Z_i^{4.62} + K^{coh}(E) Z_i^{2.86} + K^{KN}(E) Z_i \tag{4}$$

where K^{ph}, K^{coh} and K^{KN} are scanner dependent coefficients.

Equation 4 is be inserted to Eq. 3 to give:

$$\mu = \rho N_A \sum_{i=1}^{N} w_i \frac{Z_i}{M_i} \left(K^{ph}(E) Z_i^{4.62} + K^{coh}(E) Z_i^{2.86} + K^{KN}(E) Z_i \right) \tag{5}$$

Following from Eq 5, the linear attenuation coefficient of the tissue, relative to water, can be expressed as:

$$\frac{\mu}{\mu_w} = \frac{\rho}{\rho_w} \frac{\sum_{i=1}^{n} (w_i/M_i) (Z_i + Z_i^{2.86} k_1 + Z_i^{4.62} k_2)}{(w_H/M_H)(1 + k_1 + k_2) + (w_O/M_O)(8 + 8^{2.86} k_1 + 8^{4.62} k_2)} \tag{6}$$

where k_1 refers to the fraction K^{coh}/K^{KN} and k_2 to K^{ph}/K^{KN}. The subscripts w, H and O denote water, hydrogen and oxygen.

The key to the stoichiometric calibration is to find two scanner-specific coefficients k_1 and k_2. They can be determined by scanning materials of known elemental compositions and mass densities and perform a least square fit of the measured attenuation values to Eq. 6. When the coefficients are determined it is possible to predict what the CT numbers would be for any materials with known mass densities and elemental compositions. The calibration curve is finally obtained by plotting calculated CT numbers against the electron density (for use in X-ray therapy) or proton stopping power (for use in proton therapy).

3 Theory

3.1 Extraction of base material proportions

In the following sections, different methods to extract tissue compositions and their implementations with DECT data are presented.

3.1.1 Mixture rule

The independent atom approximation means that an atom in a material is not affected by the presence of any neighboring atoms. Under this approximation, μ/ρ of a mixture can be expressed as the sum of μ/ρ of the mixture components, weighted by mass. This is the so called mixture rule which is the base for the decomposition algorithms studied in this report:

$$\frac{\mu}{\rho} = \sum_i w_i \frac{\mu_i}{\rho_i} \tag{7}$$

where $w_i = m_i/m$ is the mass fraction of material i.

The cross-section, σ, for a specified target particle, reaction and incident particle is defined as the mean number of reactions divided by the incident particle fluence, Φ [34]. In the independent atom approximation, the linear attenuation coefficient, μ, can be expressed as the total cross-section per atom, σ_a, multiplied with the number of atoms per unit volume, N:

$$\mu = N\sigma_a \tag{8}$$

For a material consisting of several elements, μ can be written as the sum of the contributions from the different elemental components:

$$\mu = \sum_i N_i\sigma_i = \sum_i \mu_i \tag{9}$$

The mass attenuation coefficient is the linear attenuation coefficient divided by the mass density of the mixture, ρ:

$$\frac{\mu}{\rho} = \sum_i \frac{N_i\sigma_i}{\rho} \tag{10}$$

To this point, N_i has been used to denote the proportion of a certain element in the mixture. This term corresponds to the number of atoms per unit volume of *the mixture*. To break it down to more fundamental terms, the number of atoms per unit volume of the *pure material*, M_i, is used instead. This term is related to N_i as:

$$N_i = M_i \frac{V_i}{V} \tag{11}$$

where V_i is the volume of material i and V is the total volume of the mixture.

The mass attenuation coefficient for one element in the mixture can now be expressed as:

$$\frac{\mu_i}{\rho_i} = \frac{N_i \sigma_i}{\rho_i} = \frac{M_i \sigma_i}{\rho_i} \frac{V_i}{V} \tag{12}$$

Equation 10 can be rewritten to form an equation for μ/ρ of the mixture; the mixture rule:

$$\frac{\mu}{\rho} = \sum_i \frac{M_i \sigma_i}{\rho} \frac{V_i}{V} = \sum_i \frac{\rho_i}{\rho} \frac{V_i}{V} \frac{M_i \sigma_i}{\rho_i} = \sum_i \frac{\rho_i}{\rho} \frac{V_i}{V} \frac{\mu_i}{\rho_i} = \sum_i \frac{m_i}{m} \frac{\mu_i}{\rho_i} = \sum_i w_i \frac{\mu_i}{\rho_i} \tag{13}$$

The fourth step follows from the relation between mass, volume and density: $m = \rho V$.

It is important to note that the mixture rule is an approximation. Since that the atoms are assumed to be independent of each other, the rule neglects any differences in the molecular structure of the mixture to that of the base materials, which could influence the attenuation properties [35]. For instance, binding energies of the outermost electrons may be modified due to changes in chemical bonds. Although, these bonds are only in the magnitude of electron volts and should not considerably affect the cross-sections for photoelectric effect, incoherent scatter and pair production [36].

3.1.2 Material decomposition using mass fractions

For a material consisting of M base materials (i.e. mixture components), the mixture rule can be used to derive the proportions of each base material. For N different photon energies, E_1, ..., E_N, Eq. 13 yields N equations. The mass attenuation coefficients for the mixture can be written as:

$$\frac{\mu(E_1)}{\rho} = w_1 \frac{\mu_1(E_1)}{\rho_1} + w_2 \frac{\mu_2(E_1)}{\rho_2} + ... + w_N \frac{\mu_M(E_1)}{\rho_M} \tag{14}$$

$$\frac{\mu(E_2)}{\rho} = w_1 \frac{\mu_1(E_2)}{\rho_1} + w_2 \frac{\mu_2(E_2)}{\rho_2} + ... + w_N \frac{\mu_M(E_2)}{\rho_M} \tag{15}$$

$$...$$

$$\frac{\mu(E_N)}{\rho} = w_1 \frac{\mu_1(E_N)}{\rho_1} + w_2 \frac{\mu_2(E_N)}{\rho_2} + ... + w_M \frac{\mu_M(E_N)}{\rho_M} \tag{16}$$

These N equations can be written in a vector notation:

$$\text{Let } \vec{M} = \begin{bmatrix} \mu(E_1)/\rho \\ \mu(E_2)/\rho \\ \vdots \\ \mu(E_N)/\rho \end{bmatrix} \quad \text{and} \quad \vec{M}_i = \begin{bmatrix} \mu_i(E_1)/\rho_i \\ \mu_i(E_2)/\rho_i \\ \vdots \\ \mu_i(E_N)/\rho_i \end{bmatrix}.$$

Equations 14-16 can now be expressed as:

$$\vec{M} = w_1\vec{M}_1 + w_2\vec{M}_2 + ... + w_M\vec{M}_M \tag{17}$$

According to the law of mass conservation, the proportions of base materials add up to the mass of the mixture, i.e. the mass fractions add up to unity:

$$1 = w_1 + ... + w_{M-1} + w_M \tag{18}$$

This allows one mass fraction to be expressed with the others:

$$w_M = 1 - w_1 + ... + w_{M-1} \tag{19}$$

Each mass fraction must have a value larger than, or equal to 0, since negative masses are unphysical. The value must also be equal to, or less than 1, since no mixture component can have a mass larger than the total mixture mass.

The mass conservation relationship in Eq. 19 is used to substitute w_M in Eq. 17:

$$\begin{aligned}\vec{M} &= w_1\vec{M}_1 + w_2\vec{M}_2 + ... + (1 - w_1 - ... - w_{M-1})\,\vec{M}_M \\ &= w_1\left(\vec{M}_1 - \vec{M}_M\right) + w_2\left(\vec{M}_2 - \vec{M}_M\right) + ... + \vec{M}_M\end{aligned} \tag{20}$$

The vectors $(\vec{M}_i - \vec{M}_M)$, for $i = 1, ..., M-1$, construct a basis in a $(M-1)$ dimensional vector space. Any vector $\vec{M}$ in this vector space can be represented by a linear combination of the base vectors, $\vec{M}_i$, multiplied with corresponding coordinate, w_i.

Graphical representation using three base materials

The vector notation allows a graphical representation of the decomposition algorithm. Consider a mixture of three base materials. If μ/ρ of the mixture is taken at two different photon energies, E_1 and E_2, Eq. 20 reduces to:

$$\vec{M} = w_1\left(\vec{M}_1 - \vec{M}_3\right) + w_2\left(\vec{M}_2 - \vec{M}_3\right) + \vec{M}_3 \tag{21}$$

$$\left(\vec{M} - \vec{M}_3\right) = w_1\left(\vec{M}_1 - \vec{M}_3\right) + w_2\left(\vec{M}_2 - \vec{M}_3\right) \tag{22}$$

where $\vec{M} = \begin{bmatrix} \mu(E_1)/\rho \\ \mu(E_2)/\rho \end{bmatrix}$ corresponds to the mixture and $\vec{M}_i = \begin{bmatrix} \mu_i(E_1)/\rho_i \\ \mu_i(E_2)/\rho_i \end{bmatrix}$ corresponds to base material i.

Figure 3 shows a scatter plot with $\mu(E_1)/\rho$ at horizontal axis and $\mu(E_2)/\rho$ at the vertical. Values of μ/ρ for different tissues are plotted and those corresponding to base materials and to the mixture are marked. Also, the vectors on the right hand side of Eq. 22, $w_1(\vec{M}_1 - \vec{M}_3)$ and $w_2(\vec{M}_2 - \vec{M}_3)$, are drawn. It is seen that addition of these two vectors give the vector $(\vec{M} - \vec{M}_3)$, which corresponds to the left hand side of Eq. 22.

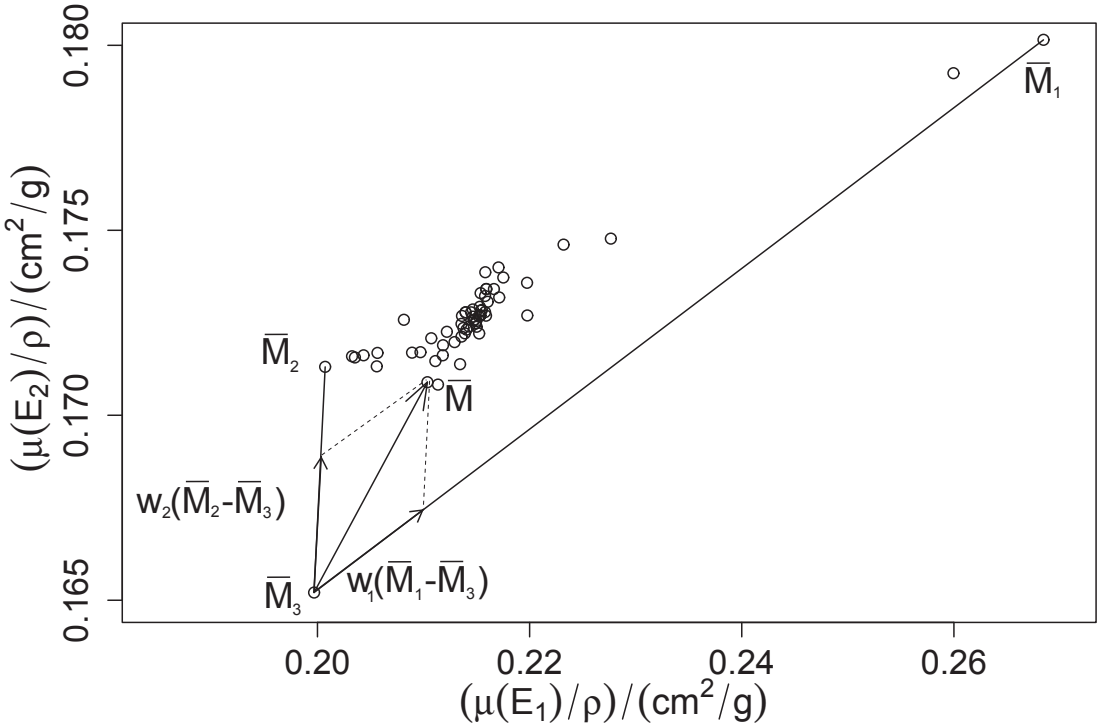

Figure 3: Graphical representation of the three-material decomposition using mass fractions.

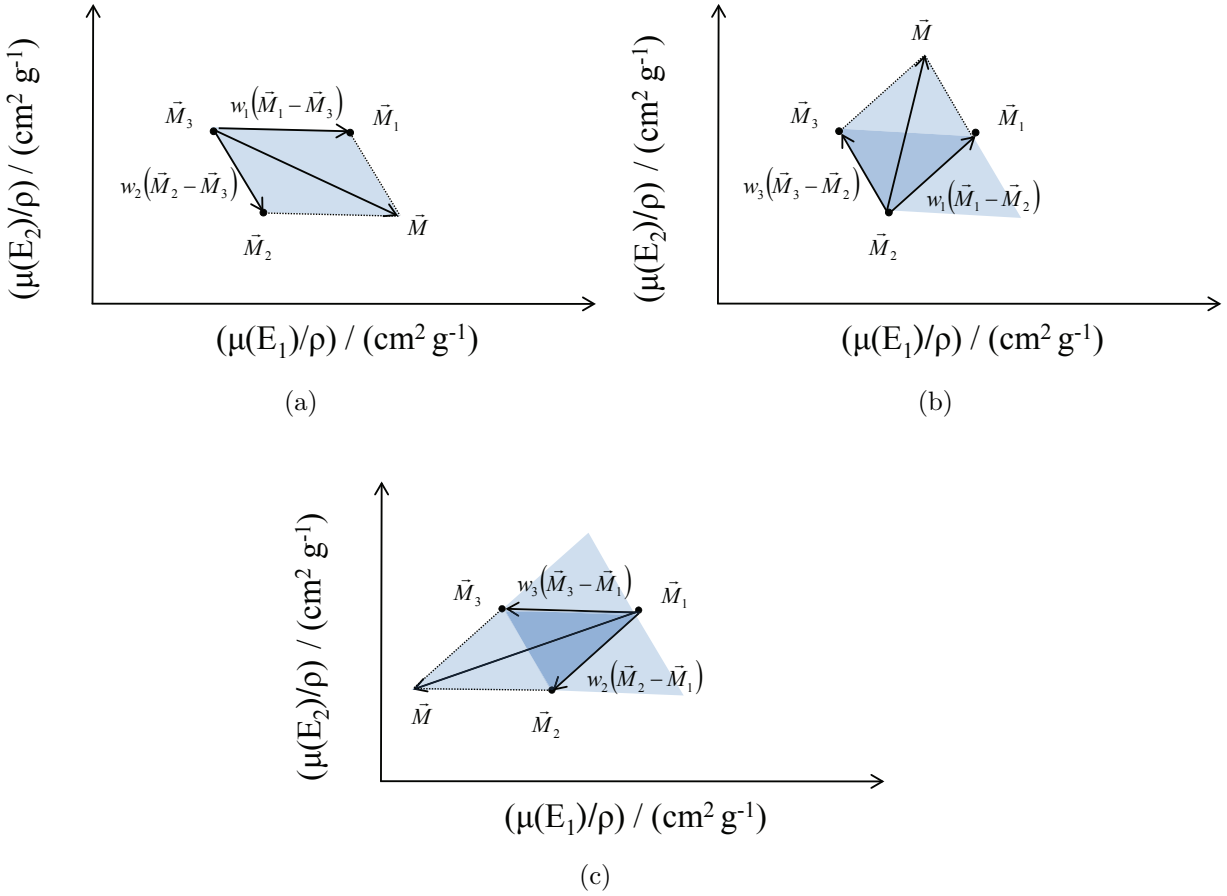

Figure 4: The figures show which values of $\vec{M}$ that are possible for all mass fractions to be positive, illustrated with vector addition of different base vectors.

The graphical representation is useful to predict the values of $\vec{M}$ that are possible to describe with a certain set of base materials. Values of each mass fraction is limited to $0 \leq w_i \leq 1$. This restricts the possible values for $\vec{M}$ to a parallelepiped given by vector addition of the two base vectors. Figure 4a show this situation for the base vectors $w_1(\vec{M}_1 - \vec{M}_3)$ and $w_2(\vec{M}_2 - \vec{M}_3)$. This follows from that w_3 is substituted with the mass conservation assumption, Eq. 19.

If instead w_2 is substituted, possible values of $\vec{M}$ will be described by vector addition of $w_3(\vec{M}_3 - \vec{M}_2)$ and $w_1(\vec{M}_1 - \vec{M}_2)$, as shown in Figure 4b. It is seen that the area spanned by the vectors only partly overlap the area in Figure 4a.

Similarly, if mass fraction w_1 is eliminated, the possible values of $\vec{M}$ is given by the vector addition shown in Figure 4c.

Consequently the values of $\vec{M}$ possible to describe with positive base material mass fractions must lie in the triangle defined by $\vec{M}_1$, $\vec{M}_2$ and $\vec{M}_3$.

3.1.3 Material decomposition with volume fractions

It is possible to describe the mixture rule in a slightly modified way. If the volumes of the base materials are conserved in the mixture, these will add up to the total volume of the mixture. In this case, volume fractions instead of mass fractions can be used to describe the proportion of each base material. The mixture rule can be modified as:

$$\mu = \rho \sum_{i=1}^{M} w_i \left(\frac{\mu}{\rho}\right)_i = \frac{m}{V} \sum_{i=1}^{M} \frac{m_i}{m} \left(\frac{V_i}{m_i}\mu_i\right) = \sum_{i=1}^{M} \frac{V_i}{V}\mu_i = \sum_{i=1}^{M} v_i \mu_i \tag{23}$$

where v_i is the volume fraction of base material i.

For a mixture consisting of M different base materials, with $\mu(E)$ taken at N different photon energies, the mixture rule yields:

$$\mu(E_1) = v_1\mu_1(E_1) + v_2\mu_2(E_1) + ... + v_M\mu_M(E_N) \tag{24}$$

$$\mu(E_2) = v_1\mu_1(E_2) + v_2\mu_2(E_2) + ... + v_M\mu_M(E_N) \tag{25}$$

$$...$$

$$\mu(E_N) = v_1\mu_1(E_N) + v_2\mu_2(E_N) + ... + v_M\mu_M(E_N) \tag{26}$$

A vector notation is introduced. Let:

$$\vec{L} = \begin{bmatrix} \mu(E_1) \\ \mu(E_2) \\ \vdots \\ \mu(E_M) \end{bmatrix} \quad \text{and} \quad \vec{L_i} = \begin{bmatrix} \mu_i(E_1) \\ \mu_i(E_2) \\ \vdots \\ \mu_i(E_M) \end{bmatrix}.$$

Equations 24-26 can now be expressed as:

$$\begin{aligned} \vec{L} &= v_1\vec{L_1} + v_2\vec{L_2} + ... + v_M\vec{L_M} \\ &= v_1\left(\vec{L_1} - \vec{L_M}\right) + v_2\left(\vec{L_2} - \vec{L_M}\right) + ... + \vec{L_M} \end{aligned} \tag{27}$$

Similar to the approach with mass fractions, any vector $\vec{L}$ can be described by a linear combination of the base vectors $(\vec{L_i} - \vec{L_M})$, multiplied with corresponding coordinate v_i. Figure 3 can be reproduced with linear attenuation coefficients replacing the mass attenuation coefficients, and volume fractions replacing the mass fractions.

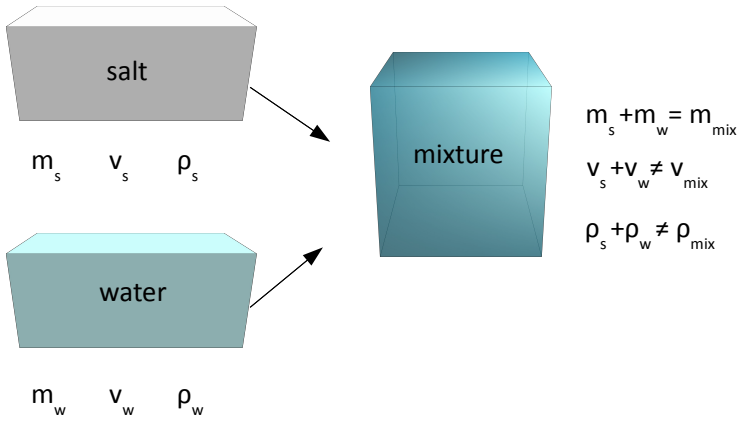

Figure 5: When solid salt and pure water is mixed, the salt will dissolve. The mass of the mixture components will be preserved, while volumes and mass density will not.

3.1.4 Physical constraints: mass or volume fractions

As described above, the mixture rule can be used to decompose a material to proportions of predefined base materials. A difference between the two approaches is the choice of physical constraint.

The volume of a material depends on e.g. chemical state, temperature and pressure, while the mass is always kept constant in any chemical reaction. Figure 5 illustrates a simple example of this. Consider an amount of solid salt and an amount of pure water. When mixed, the salt will to some degree be dissolved and the volumes of the components will not add up to the volume of the mixture. How volumes of different material components will be affected when mixed may be hard to predict and will depend on the set of base materials considered. Generally, it ought to be more correct to use mass fractions, since these are always conserved.

3.1.5 Material decomposition with mass fractions using DECT data

A DECT scan provides μ-values for two effective energies, E_1 and E_2; $\mu(E_1)$ and $\mu(E_2)$. According to the approaches described above, two measurements of $\mu(E)$ at different energies allows proportions of three base materials to be extracted.

The three base materials need to be chosen before the decomposition is performed. If elemental composition of the mixture is to be extracted, some information needs to be known of the base materials, including the elemental compositions, mass densities and μ/ρ at the concerned energy spectra.

For the two effective photon energies used in a DECT scan, mass fractions of three base materials can be extracted. The mixture rule yields:

$$\frac{\mu(E_1)}{\rho} = w_1\frac{\mu_1(E_1)}{\rho_1} + w_2\frac{\mu_2(E_1)}{\rho_2} + w_3\frac{\mu_3(E_1)}{\rho_3} \tag{28}$$

$$\frac{\mu(E_2)}{\rho} = w_1\frac{\mu_1(E_2)}{\rho_1} + w_2\frac{\mu_2(E_2)}{\rho_2} + w_3\frac{\mu_3(E_2)}{\rho_3} \tag{29}$$

Applying the mass conservation (Eq. 19) one of the mass fractions can be expressed with the other two:

$$\frac{\mu(E_1)}{\rho} = w_1\left(\frac{\mu_1(E_1)}{\rho_1} - \frac{\mu_3(E_1)}{\rho_3}\right) + w_2\left(\frac{\mu_2(E_1)}{\rho_2} - \frac{\mu_3(E_1)}{\rho_3}\right) + \frac{\mu_3(E_1)}{\rho_3} \tag{30}$$

$$\frac{\mu(E_2)}{\rho} = w_1\left(\frac{\mu_1(E_2)}{\rho_1} - \frac{\mu_3(E_2)}{\rho_3}\right) + w_2\left(\frac{\mu_2(E_2)}{\rho_2} - \frac{\mu_3(E_2)}{\rho_3}\right) + \frac{\mu_3(E_2)}{\rho_3} \tag{31}$$

In these two equations, μ-values for the mixture are provided by the DECT scan and μ-values for the base materials are assumed to be known. The aim is to find the unknown mass fractions w_1, w_2 and the mass density of the mixture, ρ. But Eqs 30 and 31 forms an underdetermined system of linear equations; there are three unknown parameters and only two equations. To be solvable, one unknown parameter needs to be eliminated or one more independent relation needs to be provided (i.e. μ-values at a third photon energy).

One way to deal with this is to apply a volume conservation criterion, i.e. the volume of the material components, V_{1-3}, add up to the total volume of the mixture, V :

$$V = V_1 + V_2 + V_3 \tag{32}$$

This criterion allows the mass density of the mixture to be expressed with the mass density of the base materials:

$$\frac{1}{\rho} = \frac{V}{m} = \frac{V_1 + V_2 + V_3}{m} = \frac{m_1}{m}\frac{V_1}{m_1} + \frac{m_2}{m}\frac{V_2}{m_2} + \frac{m_3}{m}\frac{V_3}{m_3} = w_1\frac{1}{\rho_1} + w_2\frac{1}{\rho_2} + w_3\frac{1}{\rho_3} \tag{33}$$

According to the discussion in Section 3.1.4, the volume conservation assumption may not be correct in all situations. The effect this has on the result of the decomposition is hard to predict and have to be evaluated experimentally. In order to optimize the decomposition method, a correction of the mass density may need to be introduced.

Expressing w_3 with w_2 and w_1 as before, the mass density assumption becomes:

$$\frac{1}{\rho} = w_1(\frac{1}{\rho_1} - \frac{1}{\rho_3}) + w_2(\frac{1}{\rho_2} - \frac{1}{\rho_3}) + \frac{1}{\rho_3} \tag{34}$$

This equation together with Eqs 30 and 31 establishes a system of three linear equations for which the solution is the three unknown parameters: w_1, w_2 and ρ. The third mass fraction is calculated with the mass conservation condition: $w_3 = 1 - w_1 - w_2$.

With the knowledge of the elemental composition of the base materials, it is possible to derive the elemental composition of the mixture. The mass fraction of element i, w_i^{el}, in the mixture is:

$$w_i^{el} = \sum_{i=1}^{M} w_{i,j}^{el} w_i \tag{35}$$

where w_i^{el} is the mass fraction of element i in the mixture, $w_{i,j}^{el}$ is the mass fraction of element j in base material i and w_i is the mass fraction of base material i in the mixture.

3.1.6 Material decomposition with volume fractions using DECT data

The mass density assumption (Eq. 33) implies that the volumes of the base materials are preserved in the mixture. Under this assumption, the decomposition method using mass fractions is equivalent to the method using volume fractions; the volume fractions can be converted to mass fractions without any loss of information.

As described in Section 3.1.3, a mixture of three base materials with μ known at two energies, E_1 and E_2, can be expressed as:

$$\mu(E_1) = v_1 \left[\mu_1(E_1) - \mu_3(E_1)\right] + v_2 \left[\mu_2(E_1) - \mu_3(E_1)\right] + \mu_3(E_1) \tag{36}$$

$$\mu(E_2) = v_1 \left[\mu_1(E_2) - \mu_3(E_2)\right] + v_2 \left[\mu_2(E_2) - \mu_3(E_2)\right] + \mu_3(E_2) \tag{37}$$

A DECT scan provides $\mu(E_1)$ and $\mu(E_2)$, which means that there are two equations with two unknown parameters, v_1 and v_2. When these are extracted, the third volume fraction is given by the volume conservation, Eq. 32.

3.1.7 Material decomposition with density as a free parameter using DECT

When implementing the three-material decomposition models described above with DECT, both assumes that the volume fractions are preserved in the mixture. In situations where this is clearly not fulfilled (as for instance in the salt and water mixture in Figure 5) there is a possibility to treat the mass density as a free parameter. However, in this case only proportions of two base materials can be extracted.

Consider a mixture of two base materials, with μ-values known at two photon energies, E_1 and E_2. The mixture rule yields:

$$\vec{M} = \frac{1}{\rho}\vec{L} = w_1\vec{M}_1 + w_2\vec{M}_2 = w_1\left(\vec{M}_1 - \vec{M}_2\right) + \vec{M}_2 \tag{38}$$

$$\frac{1}{\rho}\vec{L} = w_1\left(\vec{M}_1 - \vec{M}_2\right) \tag{39}$$

where the last step follows from the mass preservation assumption, $w_2 = 1 - w_1$.

For any tissue, ρ and w_1 can be extracted from Eq. 39 with values of $\mu(E)$ measured at two different photon energies. When w_1 is known, the mass fraction of the second base material is given by $w_2 = 1 - w_1$. The elemental compositions can then be derived in the same way as for the three-material decomposition methods, Eq. 35.

4 Extraction of tissue compositions

4.1 Methods

4.1.1 Elemental compositions

The International Commission on Radiation Units and Measurements (ICRU) has published typical elemental compositions for different tissue types in Report 44 and 46 [37, 38]. Elemental compositions and densities used in this work were taken from these reports and from the articles by Woodard and White [39] and White et al. [40]. The 71 selected tissues are presented in Tables 17 and 18 in Appendix A.

It is important to keep in mind that tissue compositions may vary significantly between individuals. Diet, genetics, age, sex and health status are only a few parameters that may affect the composition. In order to describe these variations, Woodard and White [39] and White et al. [40] have presented some tissue compositions in three versions. Tissue 2 represents the mean values, tissue 1 mean values minus one standard deviation and tissue 3 mean values plus 1 standard deviation.

The elemental composition for "soft tissue" was taken from the article by White et al. [40] and represents the mean values of 40 different male soft tissues.

Calcified prostate tissue

The prostate gland is prone to get calcifications. These can be expressed as small mineral infiltrations (microcalcifications) or as larger stones (calculi) [41].

The literature on composition, spread and distribution of prostate calcifications is scarce. One exception is the study by Suh et al. [41] who analyzed 298 prostate specimens obtained from operations of cancer in prostate or bladder. Different degrees of calcifications were found in 88.6% of the prostate samples. However, no quantitative measure of the degree of calcifications or any elemental compositions were reported.

No data could be found on elemental compositions of prostate calcifications. In order to study the influence of calcifications in brachytherapy, breast calcifications were used as a substitute. Data on breast calcifications were obtained from ICRU Report 46 [37]. The compositions of the calcified tissues were derived as weighted sums by mass of prostate tissue and breast calcifications. This resulted in a homogeneously calcified prostate tissue, which worked as a simple approximation to investigate the effects of calcifications. The calculated compositions for prostates with 2% and 5% calcifications are shown in Table 1.

Table 1: Composition of tabulated breast calcification [37], tabulated prostate tissue [39] and calculated homogeneously calcified prostate tissues.

		w_i (percentage by mass)								
Tissue	ρ	H	C	N	O	Na	P	S	K	Ca
Calcification	3.06	0.3	1.6	0.5	40.7	-	18.7	-	-	38.2
Prostate tissue	1.04	10.5	8.9	2.5	77.4	0.2	0.1	0.2	0.2	-
2% calcified prostate	1.08	10.3	8.8	2.5	76.7	0.2	0.5	0.2	0.2	0.8
5% calcified prostate	1.14	10.0	8.5	2.4	75.6	0.2	1.0	0.2	0.2	1.9

4.1.2 CT spectra

The Siemens Somatom Definition Flash scanner can operate at four different tube voltages; U = 80 kV, 100 kV, 120 kV and 140 kV. The highest tube voltage is possible to use with extra 0.4 mm tin filtration. The decomposition algorithms are assumed to benefit from large differences in attenuation between the base materials. Therefore, the spectra with the lowest (U=80 kV) and the highest (U = 140 kV with extra 0.4 mm tin filtration) mean energies were chosen.

The energy spectra were calculated with the software SpekCalc [42]. To achieve good agreement with spectra provided by Siemens under non-disclosure agreement, the calculated spectra were modified with aluminum filtration. The U=80 kV spectrum was calculated with 7 degrees anode angle and filtration of 10.0 mm Al and 1000 mm air. The U=140 kV spectrum was calculated with 7 degree anode angle and filtration with 8.0 mm Al, 0.4 mm Sn and 1000 mm air. Parameters for the spectra calculated with SpekCalc and spectra obtained from Siemens are compared in Table 2.

The half-value layer (x_{HVL}) corresponds to the thickness of a material that reduces the air kerma, K_{air}, of a photon beam to half the initial value. For a monoenergetic beam of energy E, the quantity can be derived from the exponential law of attenuation:

$$K_{air,x_{HVL}} = K_{air,0} e^{-\mu(E) x_{HVL}} \tag{40}$$

where $K_{air,0}$ is the initial air kerma and $K_{air,x_{HVL}}$ is the air kerma of the beam after the distance x_{HVL}.

Due to the energy dependence of μ, the transmission curve of a polychromatic beam does not follow the same, simple exponential decrease as a monochromatic beam. For the polychromatic photon beam, the initial air kerma is:

$$K_{air,0} = \int_{E=0}^{E_{max}} \left(\frac{\mu_{tr}(E)}{\rho} \right)_{air} E \Phi_E(E)\, dE \tag{41}$$

where $\Phi_E(E)$ is the distribution of photon fluence with respect to energy E and $(\mu_{tr,air}(E)/\rho)$ is the mass energy-transfer coefficient for air.

After passing a distance x in a material, e.g. aluminum, the initial air kerma is reduced to $K_{air,x}$:

$$K_{air,x} = \int_{E=0}^{E_{max}} e^{-\left(\frac{\mu(E)}{\rho}\right)_{Al}\rho_{Al}x} \left(\frac{\mu_{tr}(E)}{\rho}\right)_{air} E\Phi_E(E)\,dE \tag{42}$$

The half-value layer is the thickness that satisfies:

$$K_{air,x_{HVL}} = \frac{K_{air,0}}{2} \tag{43}$$

The resulting equation is used to numerically solve x_{HVL}:

$$\frac{1}{2} = \frac{K_{air,x_{HVL}}}{K_{air,0}} = \frac{\int_{E=0}^{E_{max}} e^{-\left(\frac{\mu(E)}{\rho}\right)_{Al}\rho_{Al}x_{HVL}} \left(\frac{\mu_{tr}(E)}{\rho}\right)_{air} \Phi_E(E)\,dE}{\int_{E=0}^{E_{max}} \left(\frac{\mu_{tr}(E)}{\rho}\right)_{air} \Phi_E(E)\,dE} \tag{44}$$

The mean energies with respect to photon fluence were calculated as:

$$\bar{E}_\Phi = \frac{\int_{E=0}^{E_{max}} E\Phi_E(E)\,dE}{\int_{E=0}^{E_{max}} \Phi_E(E)\,dE} \tag{45}$$

Similarly, the mean energies with respect to energy fluence were calculated as:

$$\bar{E}_\Psi = \frac{\int_{E=0}^{E_{max}} E\Psi_E(E)\,dE}{\int_{E=0}^{E_{max}} \Psi_E(E)\,dE} \tag{46}$$

where $\Psi_E(E)$ is the energy fluence for photons of energy E.

The two spectra calculated with SpekCalc are shown in Figure 6.

Table 2: Half-value layer and mean energies weighted by fluence and energy fluence for calculated spectra versus spectra obtained from Siemens under non-disclosure agreement. $\bar{E}_\Phi$ denotes mean energy with respect to fluence and $\bar{E}_\Psi$ mean energy with respect to energy fluence.

	U=80 kV		U=140 kV	
	SpekCalc	Siemens	SpekCalc	Siemens
x_{HVL} / mm Al.	5.7	5.8	13.2	13.3
$\bar{E}_\Phi$ / keV	51.8	51.9	88.6	88.7
$\bar{E}_\Psi$ / keV	54.5	54.6	94.3	94.0

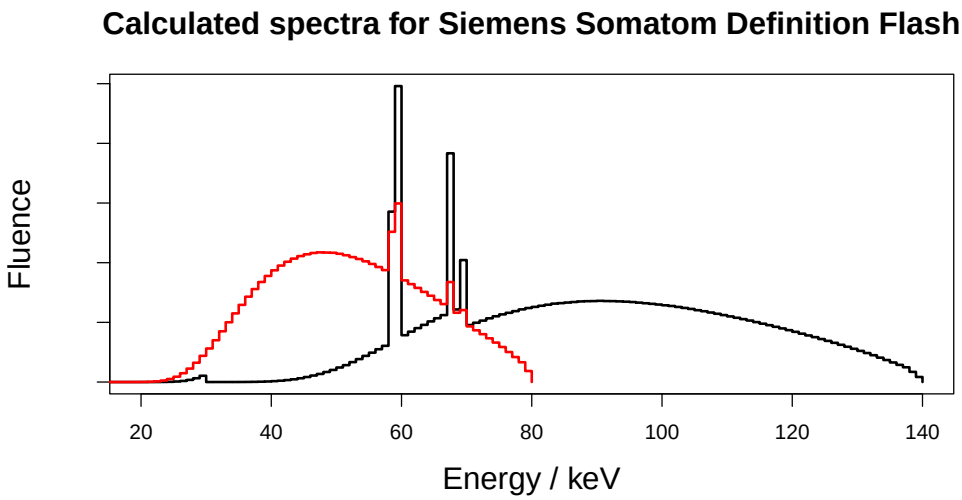

Figure 6: Calculated spectra for U = 80 kV (red) and U = 140 kV with extra 0.4 mm tin filtration (black), which were used to derive μ-values.

4.1.3 Extraction of tissue parameters

For all selected tissues, μ-values were derived at $\bar{E}_\Psi$ for the calculated U = 80 kV and U = 140 kV spectra. Photon interaction data was taken from the Evaluated Photon Data Library (1997 version) [43].

The calculated μ-values were used as input to the three-decomposition method. Soft tissues were decomposed into mass fractions of water, lipid and protein; skeletal tissues into cortical bone, red bone marrow and yellow bone marrow.

The extraction of weight fractions was performed with a MATLAB® [44] script, which is presented in Appendix B.

4.2 Results and discussion

In the following section, the three-material decomposition method using volume preservation (cf Section 3.1.6) will be referred to as the *3MDv* method and the two material decomposition with density as a free parameter (cf Section 3.1.7) will be referred to as the *2MD* method.

Figure 7 shows a scatter plot of mass attenuation coefficients for soft tissues. It is seen that the triangle defined by water, lipid and protein only covers a part of all the soft tissues. Only tissues with μ/ρ-values positioned inside the triangle will have positive mass fractions for all three base materials.

Figure 8 shows a ternary plot over the base material mass fractions, w_{base}, that were extracted for soft tissues using the 3MDv method. The proportion of each base material can be read from the position in the plot; from 1 at each apex, to 0 at the base opposite to the apex. It is seen that the dominating base materials in soft tissues are water and lipid.

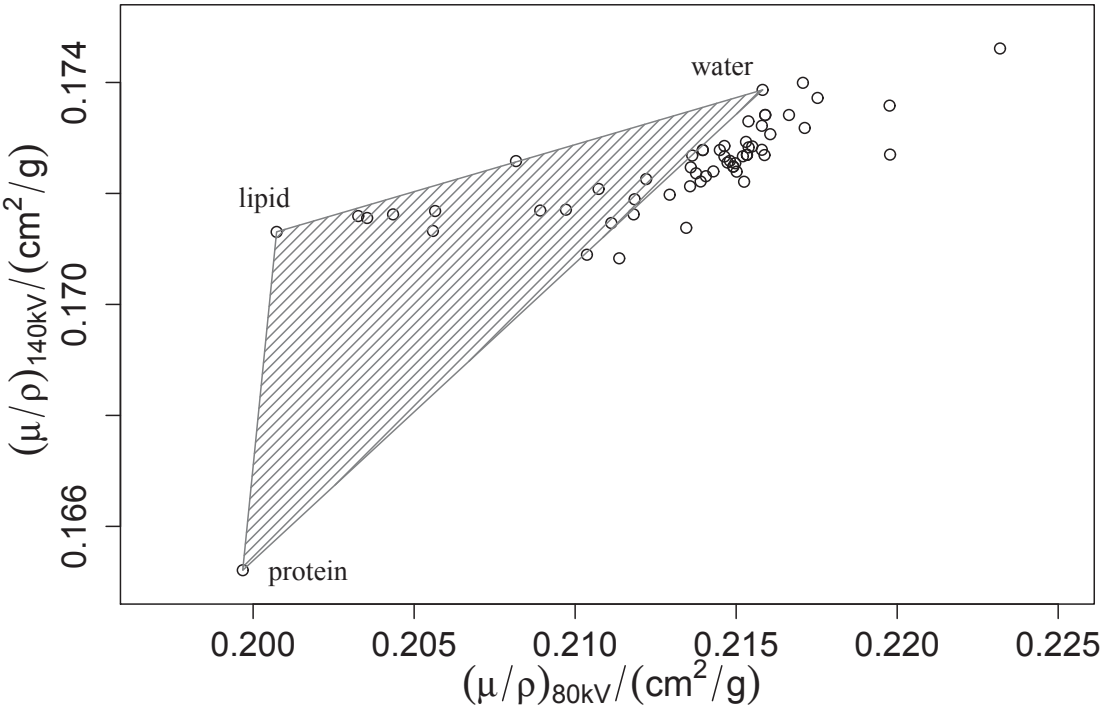

Figure 7: Scatter plot of μ/ρ of soft tissues. The triangle delimits tissues with positive mass fractions of water, lipid and protein, calculated using the 3MDv method.

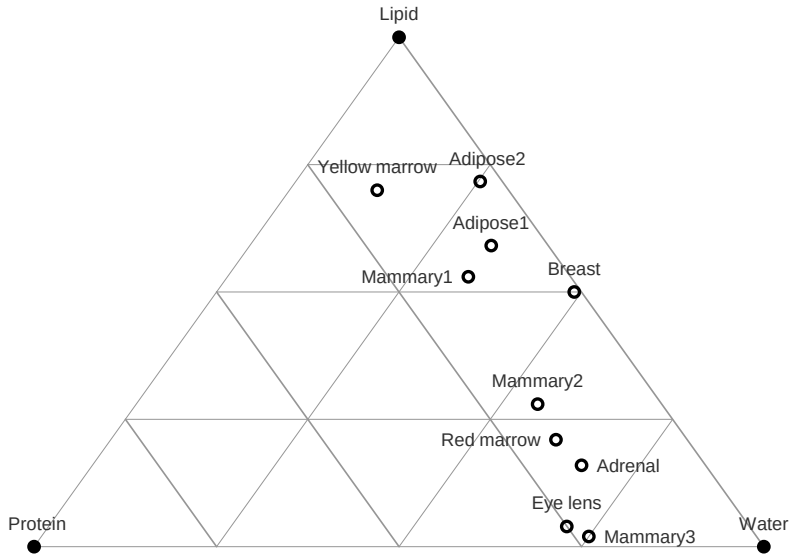

Figure 8: Ternary plot showing mass fractions of water, lipid, and protein calculated using the 3MDv method to decompose soft tissues.

Values of w_{base} are also presented in Table 3 and the extracted elemental compositions in Table 4.

Table 3: Tissues yielding non-negative base material mass fractions when decomposed into proportions of water, lipid and protein.

	w_i (by mass)		
Tissue	Water	Lipid	Protein
Adipose 1	0.33	0.59	0.08
Adipose 2	0.21	0.72	0.03
Adrenal	0.67	0.17	0.17
Breast	0.49	0.50	0.01
Eye lens	0.72	0.04	0.25
Mammary 1	0.33	0.53	0.14
Mammary 2	0.55	0.28	0.17
Mammary 3	0.75	0.03	0.23
Red marrow	0.61	0.21	0.18
Yellow marrow	0.12	0.70	0.18
“Soft tissue”	0.79	0.08	0.13

Table 4: Elemental mass fractions for tissues yielding non-negative base material mass fractions, when treated as a mixture of water, lipid and protein. Within parenthesis are the deviations from tabulated values; for elemental weights $w^{el}_{true} - w^{el}_{classified}$ (in percentage points) and for the mass density $\rho_{true} - \rho_{classified}$ (g/cm^3).

	w^{el}_i (% by mass)						
Tissue	H	C	N	O	Na	S	$\rho/[\mathrm{gcm}^3]$
Adipose 1	11.2 (0.0)	49.8 (1.9)	1.3 (-0.0)	37.6 (-2.1)	0.0 (0.1)	0.1 (0.0)	0.97 (-0.0)
Adipose 2	11.5 (-0.1)	57.1 (2.7)	0.6 (0.1)	30.9 (-3.1)	0.0 (0.1)	0.0 (0.1)	0.95 (0.0)
Adrenal	10.5 (0.1)	21.8 (6.6)	2.9 (-0.3)	64.6 (-6.8)	0.0 (0.0)	0.2 (0.0)	1.03 (-0.0)
Breast	11.5 (0.0)	39.6 (-0.8)	0.2 (-0.2)	48.8 (1.0)	0.0 (0.0)	0.0 (-0.0)	0.96 (-0.0)
Eyeless	10.1 (-0.5)	16.1 (3.4)	4.2 (1.5)	69.3 (-4.7)	0.0 (0.1)	0.3 (0.1)	1.07 (0.0)
Mammary 1	10.9 (0.0)	48.5 (2.1)	2.4 (-0.1)	38.1 (-2.3)	0.0 (0.1)	0.1 (-0.0)	0.99 (-0.0)
Mammary 2	10.6 (0.0)	30.4 (2.8)	2.9 (0.1)	56.0 (-3.2)	0.0 (0.1)	0.2 (0.0)	1.02 (0.0)
Mammary 3	10.2 (0.0)	14.1 (1.7)	3.9 (-0.2)	71.6 (-1.8)	0.0 (0.1)	0.2 (-0.0)	1.06 (-0.0)
Red marrow	10.5 (0.0)	25.5 (15.9)	3.1 (0.3)	60.7 (-16.8)	0.0 (0.0)	0.2 (0.0)	1.03 (0.0)
Yellow marrow	10.8 (0.7)	64.1 (0.3)	3.1 (-2.4)	21.9 (1.2)	0.0 (0.1)	0.2 (-0.1)	0.99 (0.0)
”Soft tissue”	10.6 (-0.1)	13.0 (12.6)	2.3 (0.5)	74.0 (-13.8)	0.0 (0.1)	0.1 (0.1)	1.03 (0.0)

As seen in Table 4, the errors of the extracted elemental compositions were relatively small for hydrogen (up to -0.5 percentage points (pp)), sodium (up to 0.1 pp) and sulfur (up to 0.1 pp). The mass densities were determined with a maximum error of 0.02 g/cm^3 ("soft tissue"). Larger errors were seen for carbon (up to 15.9 pp), nitrogen (up to -2.9 pp) and oxygen (up to -16.8 pp). The errors for carbon and oxygen in each tissue tended to counterbalance, so that the sum of carbon and oxygen could be accurately determined even though the individual proportions deviated significantly.

Several of the investigated soft tissues contained small amounts of elements of high atomic numbers; chlorine, phosphorus, potassium, iron, calcium and iodine. Since these elements are not present in water, lipid or protein, they could not be accounted for. For example, red bone marrow contains 0.1% phosphorus (Z=15), 0.2% chlorine (Z=17), 0.2% potassium (Z=19) and 0.1% iron (Z=26). The inability to account for these elements may have caused the shift in mass fractions from carbon (underestimated with 15.9 pp) to oxygen (overestimated with 16.8 pp).

When the elemental compositions were derived, several tissues with negative base material mass fractions showed positive elemental weights. One of these tissues was prostate that had a negative value for lipid:

$$w_{water} = 0.93, \quad w_{lipid} = -0.06, \quad w_{protein} = 0.13$$

When the elemental composition for prostate was derived, the negative contributions from lipid for each element were subtracted from the contributions from water and protein. Since the negative value was relatively small, the elemental composition still ended up with positive values.

Tissues with negative values of w_{base}, but positive elemental compositions, are listed in Table 5 and the elemental compositions in Table 6. The errors in the elemental compositions were in general slightly larger than the tissues having positive w_{base}. The largest error for hydrogen was -0.4 pp (skeletal muscle 1), carbon 17.5 pp (white brain matter), nitrogen -1.5 pp (bile), oxygen -19.2 pp (white brain matter), sodium 0.6 pp (connective tissue), and sulfur 0.2 pp (e.g. connective tissue).

Table 5: Tissues yielding negative base material mass fractions, but positive elemental compositions, when decomposed to water, lipid and protein.

	w_i (by mass)		
Tissue	Water	Lipid	Protein
Brain, white matter	0.94	-0.06	0.13
Bile	0.97	-0.06	0.09
Connective	0.74	-0.11	0.37
GI-tract	0.90	-0.01	0.11
Heart 1	0.90	-0.06	0.16
Heart 2	0.94	-0.09	0.15
Kidney 1	0.93	-0.08	0.15
Skeletal muscle 1	0.91	-0.06	0.15
Skeletal muscle 2	0.95	-0.09	0.14
Pancreas	0.86	-0.01	0.15
Prostate	0.93	-0.06	0.13
Skin 1	0.68	-0.00	0.33
Skin 2	0.73	-0.04	0.31
Skin 3	0.79	-0.09	0.30
Stomach	0.86	-0.04	0.17
Trachea	0.91	-0.09	0.18

Table 6: Extracted parameters for tissues yielding negative base material mass fractions, but positive elemental compositions. Within parenthesis is the deviation from true values; for elemental weights $w^{el}_{true} - w^{el}_{classified}$ (percentage points), and for the mass density $\rho_{true} - \rho_{classified}$ (g/cm^3).

	w_i^{el} (% by mass)						
Tissue	H	C	N	O	Na	S	$\rho/[\mathrm{gcm}^3]$
White br. mat.	10.6 (0.0)	1.9 (17.5)	2.1 (0.4)	85.3 (-19.2)	0.0 (0.2)	0.1 (0.1)	1.04 (0.0)
Bile	10.7 (0.1)	0.0 (6.1)	1.6 (-1.5)	87.6 (-5.4)	0.0 (0.4)	0.1 (-0.1)	1.03 (-0.0)
Connective	9.4 (-0.0)	11.3 (9.4)	6.4 (-0.2)	72.5 (-10.3)	0.0 (0.6)	0.4 (0.2)	1.12 (0.0)
GI-tract	10.7 (-0.1)	5.3 (6.2)	1.8 (0.4)	82.1 (-7.0)	0.0 (0.1)	0.1 (-0.0)	1.03 (0.0)
Heart 1	10.4 (-0.1)	4.2 (13.3)	2.7 (0.4)	82.5 (-14.4)	0.0 (0.1)	0.2 (0.0)	1.05 (0.0)
Heart 2	10.5 (-0.1)	0.8 (13.1)	2.5 (0.4)	86.1 (-14.3)	0.0 (0.1)	0.2 (0.1)	1.05 (0.0)
Kidney 1	10.5 (-0.3)	1.6 (14.4)	2.5 (0.9)	85.3 (-16.0)	0.0 (0.2)	0.2 (0.1)	1.05 (0.0)
Sk. muscle 1	10.5 (-0.4)	3.4 (13.7)	2.6 (1.0)	83.4 (-15.3)	0.0 (0.1)	0.2 (0.1)	1.05 (0.0)
Sk. muscle 2	10.5 (-0.3)	0.7 (13.6)	2.5 (1.0)	86.2 (-15.2)	0.0 (0.1)	0.1 (0.2)	1.05 (0.0)
Pancreas	10.5 (0.1)	7.4 (9.5)	2.5 (-0.3)	79.4 (-10.0)	0.0 (0.1)	0.2 (0.1)	1.04 (-0.0)
Prostate	10.6 (-0.1)	2.2 (6.7)	2.1 (0.4)	84.9 (-7.5)	0.0 (0.2)	0.1 (0.1)	1.04 (0.0)
Skin 1	9.7 (0.3)	17.2 (7.9)	5.5 (-0.9)	67.3 (-7.9)	0.0 (0.2)	0.3 (-0.0)	1.09 (-0.0)
Skin 2	9.7 (0.3)	13.7 (6.7)	5.3 (-1.1)	71.0 (-6.5)	0.0 (0.2)	0.3 (-0.1)	1.09 (-0.0)
Skin 3	9.8 (0.3)	9.0 (6.8)	5.1 (-1.4)	75.9 (-6.4)	0.0 (0.2)	0.3 (-0.1)	1.09 (-0.0)
Stomach	10.4 (0.0)	6.4 (7.5)	2.9 (-0.0)	80.1 (-8.0)	0.0 (0.1)	0.2 (0.0)	1.05 (0.0)
Trachea	10.3 (-0.2)	2.5 (11.4)	3.1 (0.2)	83.9 (-12.6)	0.0 (0.1)	0.2 (0.2)	1.06 (0.0)

The 3MDv method was also applied to skeletal tissues, using the base materials cortical bone, red bone marrow and yellow bone marrow. Figure 9 shows a scatter plot over μ/ρ-values with the triangle defined by the base materials. The triangle is sharper than that for soft tissues, which may indicate that the decomposition could be more susceptible to variations in elemental compositions and corrupt DECT data.

Figure 10 shows a ternary plot for the skeletal tissues yielding positive w_{base}. Quantitative values are presented in Table 7 and the extracted elemental compositions in Table 8.

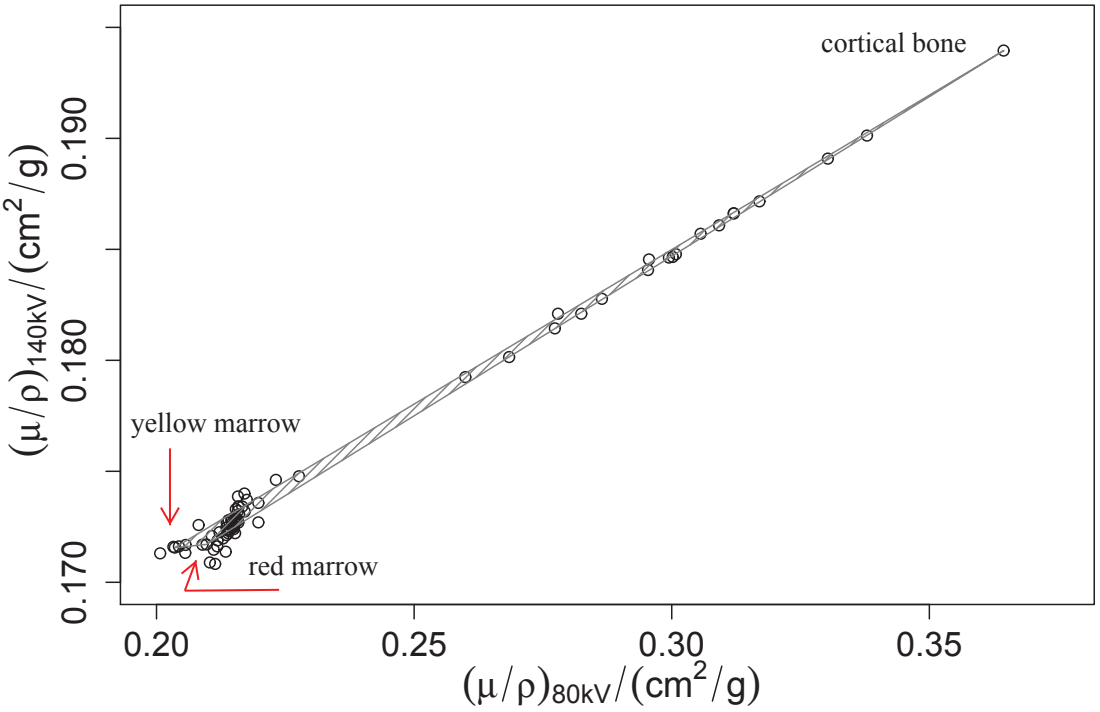

Figure 9: Scatter plot for μ/ρ values for skeletal tissues. The triangle shows which tissues that are possible to decompose into positive mass fractions of cortical bone, red and yellow bone marrow.

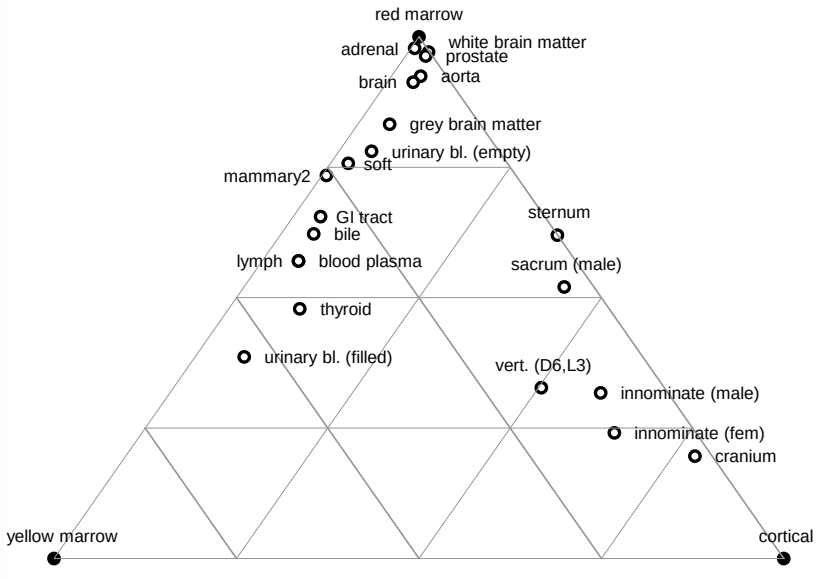

Figure 10: Ternary plot showing mass fractions of cortical bone, red bone marrow and yellow bone marrow.

Table 7: Tissues yielding positive base material mass fractions when treated as mixtures of cortical bone, red marrow and yellow marrow. Skeletal tissues are emphasized with bold text.

	w_i (by mass)		
Tissue	Cortical bone	Red marrow	Yellow marrow
Adrenal	0.01	0.98	0.02
Aorta	0.04	0.92	0.04
Bile	0.04	0.62	0.33
Blood, plasma	0.05	0.57	0.38
Brain, grey matter	0.04	0.83	0.12
Brain	0.04	0.91	0.05
Brain, white matter	0.03	0.97	0.00
GI-tract	0.04	0.66	0.31
Lymph	0.05	0.57	0.38
Mammary 2	0.01	0.73	0.26
Prostate	0.03	0.96	0.01
Cranium	**0.78**	**0.20**	**0.02**
Innominate (female)	**0.65**	**0.24**	**0.11**
Innominate (male)	**0.59**	**0.32**	**0.09**
Sacrum (male)	**0.44**	**0.52**	**0.04**
Sternum	**0.38**	**0.62**	**0.00**
Vert. (D6. L3)	**0.50**	**0.33**	**0.17**
Soft	0.02	0.76	0.22
Thyroid	0.10	0.48	0.42
Urinary bladder, empty	0.04	0.78	0.17
Urinary bladder, filled	0.07	0.39	0.55

It is seen that not only skeletal tissues but also several soft tissues could be described with the considered base materials. Since soft tissues are not composed of cortical bone, red marrow and yellow marrow, the relatively large errors seen in Table 8 are not surprising. The errors were up to -48.7 pp for carbon and up to 50.5 pp for oxygen (filled urinary bladder). The results for the skeletal tissues were in better agreement with tabulated values. The largest error was 3.5 pp (carbon and oxygen in vertebral column, D6 L3). The mass densities were in agreement with tabulated values for all tissues that were possible to describe with non-negative w_{base}.

Table 8: Extracted parameters for tissues yielding positive w_{base}, when treated as mixtures of cortical bone, red bone marrow and yellow bone marrow. Within parenthesis is the deviation from tabulated values; for elemental weights $w^{el}_{true} - w^{el}_{classified}$ (percentage points), and for the mass density $\rho_{true} - \rho_{classified}$ (g/cm^3). Skeletal tissues are emphasized with bold text.

	w_i^{el} (% by mass)						
Tissue	H	C	N	O	Na	S	Cl
Adrenal	10.5 (0.1)	41.7 (-13.3)	3.4 (-0.8)	43.5 (14.3)	0.0 (0.0)	0.2 (0.0)	0.2 (0.0)
Aorta	10.2 (-0.3)	41.2 (-26.5)	3.3 (0.9)	43.2 (26.6)	0.0 (0.2)	0.2 (0.1)	0.2 (-0.2)
Bile	10.5 (0.3)	47.9 (-41.8)	2.5 (-2.4)	37.0 (45.2)	0.0 (0.4)	0.2 (-0.2)	0.2 (0.2)
Blood, plasma	10.5 (0.3)	48.8 (-44.7)	2.4 (-1.3)	36.0 (47.2)	0.0 (0.3)	0.2 (-0.1)	0.2 (0.2)
Brain, grey matter	10.3 (0.4)	41.7 (-33.6)	3.3 (-1.3)	42.8 (35.4)	0.0 (0.2)	0.2 (0.0)	0.2 (0.1)
Brain	10.3 (0.4)	40.7 (-27.2)	3.4 (-1.1)	43.9 (28.4)	0.0 (0.2)	0.2 (0.0)	0.2 (0.1)
Brain, white matter	10.5 (0.3)	47.5 (-21.3)	2.6 (-0.9)	37.5 (22.2)	0.0 (0.2)	0.2 (0.0)	0.2 (0.1)
GI-tract	10.5 (0.1)	47.5 (-36.0)	2.6 (-0.4)	37.5 (37.6)	0.0 (0.1)	0.2 (-0.1)	0.2 (0.0)
Lymph	10.5 (0.3)	48.8 (-44.7)	2.4 (-1.3)	36.0 (47.2)	0.0 (0.3)	0.2 (-0.1)	0.2 (0.2)
Mammary 2	10.7 (-0.1)	47.2 (-14.0)	2.7 (0.3)	38.5 (14.3)	0.0 (0.1)	0.2 (0.0)	0.2 (-0.1)
Prostate	10.3 (0.2)	40.9 (-32.0)	3.4 (-0.9)	43.7 (33.7)	0.0 (0.2)	0.2 (0.0)	0.2 (-0.2)
Cranium	**5.0 (0.0)**	**21.7 (-0.5)**	**4.0 (0.0)**	**43.1 (0.4)**	**0.1 (0.0)**	**0.3 (0.0)**	**0.0 (0.0)**
Innominate (female)	**6.0 (0.0)**	**27.2 (-2.2)**	**3.6 (0.3)**	**41.3 (2.2)**	**0.1 (0.0)**	**0.3 (0.0)**	**0.1 (0.0)**
Innominate (male)	**6.0 (-0.1)**	**27.2 (-2.0)**	**3.6 (0.3)**	**41.3 (1.9)**	**0.1 (0.0)**	**0.3 (0.1)**	**0.1 (0.0)**
Sacrum (male)	**7.4 (0.0)**	**31.0 (-0.8)**	**3.6 (0.1)**	**42.9 (0.9)**	**0.0 (0.0)**	**0.2 (0.0)**	**0.1 (0.0)**
Sternum	**7.8 (0.0)**	**31.6 (0.0)**	**3.7 (0.0)**	**43.7 (0.1)**	**0.0 (0.0)**	**0.2 (0.0)**	**0.1 (0.0)**
Vert. (D6. L3)	**7.1 (-0.0)**	**32.2 (-3.5)**	**3.3 (0.5)**	**40.2 (3.5)**	**0.1 (-0.1)**	**0.2 (0.0)**	**0.1 (0.0)**
Soft	10.5 (0.0)	45.8 (-20.2)	2.8 (-0.1)	39.4 (20.8)	0.0 (0.1)	0.2 (0.0)	0.2_(0.0)
Thyroid	10.2 (0.2)	48.6 (-36.7)	2.3 (0.1)	35.0 (39.5)	0.1 (0.1)	0.2 (-0.1)	0.1 (0.1)
Urinarybl., empty	10.4 (0.1)	44.3 (-34.7)	3.0 (-0.4)	40.2 (35.9)	0.0 (0.2)	0.2 (0.0)	0.2 (0.1)
Urinarybl., filled	10.6 (0.2)	52.2 (-48.7)	2.0 (-0.5)	32.5 (50.5)	0.1 (0.2)	0.2 (-0.1)	0.1 (0.4)

Table 8 cont.	w_i^{el} (% by mass)						
Tissue	P	K	Fe	Ca	Mg	I	$\rho/[\mathrm{gcm}^3]$
Adrenal	0.2 (-0.1)	0.2 (-0.1)	0.1 (-0.1)	0.1 (-0.1)	0.0 (0.0)	0.0 (0.0)	1.03 (0.0)
Aorta	0.5 (-0.1)	0.2 (-0.1)	0.1 (-0.1)	0.9 (-0.5)	0.0 (0.0)	0.0 (0.0)	1.05 (0.0)
Bile	0.5 (-0.5)	0.1 (-0.1)	0.1 (-0.1)	1.0 (-1.0)	0.0 (0.0)	0.0 (0.0)	1.03 (0.0)
Blood, plasma	0.6 (-0.6)	0.1 (-0.1)	0.1 (-0.1)	1.1 (-1.1)	0.0 (0.0)	0.0 (0.0)	1.03 (0.0)
Brain, grey matter	0.5 (-0.2)	0.2 (0.1)	0.1 (-0.1)	1.0 (-1.0)	0.0 (0.0)	0.0 (0.0)	1.04 (0.0)
Brain	0.5 (-0.1)	0.2 (0.1)	0.1 (-0.1)	0.8 (-0.8)	0.0 (0.0)	0.0 (0.0)	1.04 (0.0)
Brain, white matter	0.4 (0.0)	0.2 (0.1)	0.1 (-0.1)	0.6 (-0.6)	0.0 (0.0)	0.0 (0.0)	1.04 (0.0)
GI-tract	0.5 (-0.4)	0.1 (0.0)	0.1 (-0.1)	0.8 (-0.8)	0.0 (0.0)	0.0 (0.0)	1.03 (0.0)
Lymph	0.6 (-0.6)	0.1 (-0.1)	0.1 (-0.1)	1.1 (-1.1)	0.0 (0.0)	0.0 (0.0)	1.03 (0.0)
Mammary 2	0.1 (0.0)	0.1 (-0.1)	0.1 (-0.1)	0.1 (-0.1)	0.0 (0.0)	0.0 (0.0)	1.02 (0.0)
Prostate	0.4 (-0.3)	0.2 (0.0)	0.1 (-0.1)	0.6 (-0.6)	0.0 (0.0)	0.0 (0.0)	1.04 (0.0)
Cranium	**8.1 (0.0)**	**0.0 (0.0)**	**0.0 (0.0)**	**17.6 (0.0)**	**0.2 (0.0)**	**0.0 (0.0)**	**1.61 (0.0)**
Innominate (female)	**6.7 (-0.1)**	**0.0 (0.1)**	**0.0 (0.1)**	**14.6 (-0.3)**	**0.1 (-0.1)**	**0.0 (0.0)**	**1.46 (0.0)**
Innominate (male)	**6.7 (-0.1)**	**0.0 (0.1)**	**0.0 (0.1)**	**14.6 (-0.3)**	**0.1 (-0.1)**	**0.0 (0.0)**	**1.41 (0.0)**
Sacrum (male)	**4.6 (0.0)**	**0.1 (0.0)**	**0.1 (0.0)**	**9.9 (0.1)**	**0.1 (0.0)**	**0.0 (0.0)**	**1.29 (0.0)**
Sternum	**4.0 (0.0)**	**0.1 (0.0)**	**0.1 (0.0)**	**8.5 (0.0)**	**0.1 (0.0)**	**0.0 (0.0)**	**1.25 (0.0)**
Vert. (D6. L3)	**5.2 (-0.1)**	**0.1 (0.0)**	**0.0 (0.1)**	**11.3 (-0.2)**	**0.1 (0.0)**	**0.0 (0.0)**	**1.33 (0.0)**
Soft	0.3 (-0.1)	0.2 (0.0)	0.1 (-0.1)	0.6 (-0.6)	0.0 (0.0)	0.0 (0.0)	1.03 (0.0)
Thyroid	1.1 (-1.0)	0.1 (0.0)	0.0 (0.0)	2.2 (-2.2)	0.0 (0.0)	0.0 (0.1)	1.05 (0.0)
Urinarybl., empty	0.5 (-0.3)	0.2 (0.1)	0.1 (-0.1)	1.0 (-1.0)	0.0 (0.0)	0.0 (0.0)	1.04 (0.0)
Urinarybl, filled	0.7 (-0.6)	0.1 (0.1)	0.0 (0.0)	1.5 (-1.5)	0.0 (0.0)	0.0 (0.0)	1.03 (0.0)

Table 9: Tissues yielding negative base material mass fractions, but positive elemental composition, with the base materials cortical bone, red marrow and yellow marrow. Skeletal tissues are emphasized with bold text.

	w_i (by mass)		
Tissue	Cortical bone	Red marrow	Yellow marrow
Blood	0.02	1.44	-0.46
Brain, csf	0.09	-0.24	1.15
Heart 1	0.01	1.31	-0.32
Heart 2	0.02	1.28	-0.30
Heart 3	0.02	1.21	-0.23
Kidney 1	0.02	1.22	-0.24
Kidney 2	0.02	1.21	-0.23
Kidney 3	0.02	1.20	-0.22
Liver1	0.02	1.21	-0.23
Lung, deflated	0.03	1.15	-0.18
Skeletal musc. 1	0.01	1.23	-0.25
Skeletal musc. 2	0.02	1.22	-0.24
Skeletal musc. 3	0.02	1.15	-0.18
Ovary	0.02	1.28	-0.30
Mandible	**0.82**	**0.28**	**-0.11**
Ribs (10th)	**0.69**	**0.36**	**-0.05**
Ribs (2nd. 6th)	**0.58**	**0.46**	**-0.04**
Sacrum (female)	**0.55**	**0.56**	**-0.11**
Vert. (C4)	**0.59**	**0.47**	**-0.06**
Vert. (whole)	**0.46**	**0.83**	**-0.29**
Stomach	0.00	1.40	-0.41

As for the decomposition of soft tissues, several tissues that got negative w_{base} values was converted to positive elemental compositions. Values of w_{base} for these tissues are listed in Table 9 and the resulting elemental compositions in Table 10. The errors for the skeletal tissues were less than 2.5 pp for all elements. The large errors that are seen for soft tissues are not surprising since the base materials were not chosen with respect to these tissues.

Positive elemental compositions were possible to extract for in total 12 out of 19 skeletal tissues with a largest error of 3.5 pp. Of the 7 tissues that yielded negative elemental compositions, no mass fraction was less than -0.01% and could probably be set to zero without significantly affecting the results of Monte Carlo radiation treatment planning.

Table 10: Extracted parameters for tissues yielding negative w_{base} values, but positive elemental compositions, for the 3MDv method using cortical bone, red marrow and yellow marrow. Within parenthesis is the deviation from tabulated values; for elemental weights $w^{el}_{true} - w^{el}_{classified}$ (percentage points), and for the mass density $\rho_{true} - \rho_{classified}$ (g/cm^3). Skeletal tissues are emphasized with bold text.

	w_i^{el} (% by mass)						
Tissue	H	C	N	O	Na	S	Cl
Blood	9.9 (0.3)	30.5 (-19.5)	4.6 (-1.3)	53.4 (21.1)	0.0 (0.1)	0.2 (0.0)	0.2 (0.1)
Brain, csf	11.0 (0.1)	65.5 (-65.5)	0.4 (-0.4)	19.9 (68.1)	0.1 (0.4)	0.1 (-0.1)	0.1 (0.3)
Heart 1	10.1 (0.2)	33.7 (-16.5)	4.3 (-1.2)	50.7 (17.4)	0.0 (0.1)	0.2 (0.0)	0.2 (0.0)
Heart 2	10.1 (0.3)	34.1 (-20.2)	4.2 (-1.3)	50.1 (21.7)	0.0 (0.1)	0.2 (0.0)	0.2 (0.0)
Heart 3	10.1 (0.3)	35.5 (-25.2)	4.0 (-1.3)	48.7 (26.9)	0.0 (0.1)	0.2 (0.0)	0.2 (0.0)
Kidney 1	10.1 (0.1)	35.4 (-19.4)	4.1 (-0.7)	48.9 (20.4)	0.0 (0.2)	0.2 (0.0)	0.2 (0.0)
Kidney 2	10.1 (0.2)	35.6 (-22.4)	4.0 (-1.0)	48.6 (23.8)	0.0 (0.2)	0.2 (0.0)	0.2 (0.0)
Kidney 3	10.1 (0.3)	35.7 (-25.1)	4.0 (-1.3)	48.5 (26.7)	0.0 (0.2)	0.2 (0.0)	0.2 (0.0)
Liver 1	10.1 (0.2)	35.6 (-20.0)	4.0 (-1.3)	48.6 (21.5)	0.0 (0.2)	0.2 (0.0)	0.2 (0.0)
Lung, deflated	10.1 (0.2)	36.6 (-26.1)	3.9 (-0.8)	47.6 (27.3)	0.0 (0.2)	0.2 (0.1)	0.2 (0.1)
Skeletal musc. 1	10.1 (0.0)	35.3 (-18.2)	4.1 (-0.5)	49.1 (19.0)	0.0 (0.1)	0.2 (-0.1)	0.2 (-0.1)
Skeletal musc. 2	10.1 (0.1)	35.5 (-21.2)	4.1 (-0.7)	48.8 (22.2)	0.0 (0.1)	0.2 (-0.1)	0.2 (-0.1)
Skeletal musc. 3	10.1 (0.1)	36.7 (-25.5)	3.9 (-0.9)	47.6 (26.9)	0.0 (0.1)	0.2 (-0.1)	0.2 (-0.1)
Ovary	10.1 (0.4)	34.1 (-24.8)	4.2 (-1.8)	50.0 (26.8)	0.0 (0.0)	0.2 (0.0)	0.2 (0.0)
Mandible	**4.5 (0.1)**	**17.6 (2.3)**	**4.3 (-0.2)**	**45.8 (-2.3)**	**0.1 (0.0)**	**0.1 (0.0)**	**0.0 (0.0)**
Ribs (10th)	**5.5 (0.1)**	**22.4 (1.1)**	**4.1 (-0.1)**	**44.6 (-1.2)**	**0.1 (0.0)**	**0.1 (0.0)**	**0.1 (0.0)**
Ribs (2nd. 6th)	**6.4 (0.0)**	**25.6 (0.7)**	**4.0 (-0.1)**	**44.4 (-0.8)**	**0.1 (0.0)**	**0.1 (0.0)**	**0.1 (0.0)**
Sacrum (female)	**6.5 (0.1)**	**24.7 (2.4)**	**4.1 (-0.3)**	**45.9 (-2.4)**	**0.0 (0.1)**	**0.0 (0.0)**	**0.1 (0.0)**
Vert. (C4)	**6.3 (0.0)**	**24.9 (1.2)**	**4.0 (-0.1)**	**44.9 (-1.3)**	**0.1 (0.0)**	**0.1 (0.0)**	**0.1 (0.0)**
Vert. (whole)	**7.0 (0.1)**	**23.0 (2.8)**	**4.5 (-0.9)**	**49.7 (-2.5)**	**0.0 (0.1)**	**0.0 (0.0)**	**0.1 (0.0)**
Stomach	10.1 (0.3)	31.9 (-18.0)	4.5 (-1.6)	52.4 (19.7)	0.0 (0.1)	0.2 (0.0)	0.2 (-0.1)

Table 10 cont.	w_i^{el} (% by mass)					
Tissue	P	K	Fe	Ca	Mg	ρ/ [gcm^3]
Blood	0,3 (-0.2)	0.3 (-0.1)	0.1 (0.0)	0.4 (-0.4)	0.0 (0.0)	1.06 (0.0)
Brain, csf	0.9 (-0.9)	0.0 (0.0)	0.0 (0.0)	2.0 (-2.0)	0.0 (0.0)	1.01 (0.0)
Heart1	0.2 (0.0)	0.3 (0.0)	0.1 (-0.1)	0.2 (-0.2)	0.0 (0.0)	1.05 (0.0)
Heart 2	0.3 (-0.1)	0.3 (0.0)	0.1 (-0.1)	0.3 (-0.3)	0.0 (0.0)	1.05 (0.0)
Heart 3	0.4 (-0.2)	0.2 (0.1)	0.1 (-0.1)	0.5 (-0.5)	0.0 (0.0)	1.05 (0.0)
Kidney 1	0.3 (-0.1)	0.2 (0.0)	0.1 (-0.1)	0.4 (-0.3)	0.0 (0.0)	1.05 (0.0)
Kidney 2	0.3 (-0.1)	0.2 (0.0)	0.1 (-0.1)	0.5 (-0.4)	0.0 (0.0)	1.05 (0.0)
Kidney 3	0.4 (-0.2)	0.2 (0.0)	0.1 (-0.1)	0.5 (-0.4)	0.0 (0.0)	1.05 (0.0)
Liver 1	0.3 (0.0)	0.2 (0.1)	0.1 (-0.1)	0.5 (-0.5)	0.0 (0.0)	1.05 (0.0)
Lung. defl.	0.4 (-0.2)	0.2 (0.0)	0.1 (-0.1)	0.6 (-0.6)	0.0 (0.0)	1.05 (0.0)
Skel. musc. 1	0.3 (-0.3)	0.2 (0.2)	0.1 (-0.1)	0.3 (-0.3)	0.0 (0.0)	1.05 (0.0)
Skel. musc. 2	0.3 (-0.3)	0.2 (0.2)	0.1 (-0.1)	0.4 (-0.4)	0.0 (0.0)	1.05 (0.0)
Skel. musc. 3	0.4 (-0.4)	0.2 (0.2)	0.1 (-0.1)	0.6 (-0.6)	0.0 (0.0)	1.05 (0.0)
Ovary	0.3 (-0.1)	0.3 (-0.1)	0.1 (-0.1)	0.4 (-0.4)	0.0 (0.0)	1.05 (0.0)
Mandible	**8.5 (0.1)**	**0.1 (-0.1)**	**0.0 (0.0)**	**18.5 (0.2)**	**0.2 (0.0)**	**1.68 (0.0)**
Ribs (10th)	**7.2 (0.0)**	**0.1 (0.0)**	**0.0 (0.0)**	**15.5 (0.1)**	**0.1 (0.0)**	**1.52 (0.0)**
Ribs (2nd. 6th)	**6.0 (0.0)**	**0.1 (0.0)**	**0.0 (0.0)**	**13.0 (0.1)**	**0.1 (0.0)**	**1.41 (0.0)**
Sacrum (fem.)	**5.7 (0.1)**	**0.1 (0.0)**	**0.1 (-0.1)**	**12.3 (0.2)**	**0.1 (0.0)**	**1.39 (0.0)**
Vert. (C4)	**6.1 (0.0)**	**0.1 (0.0)**	**0.0 (0.0)**	**13.2 (0.1)**	**0.1 (0.0)**	**1.42 (0.0)**
Vert. (whole)	**4.8 (0.3)**	**0.2 (-0.1)**	**0.1 (-0.1)**	**10.3 (-0.2)**	**0.1 (0.0)**	**1.33 (0.0)**
Stomach	0.2 (-0.1)	0.3 (-0.1)	0.1 (-0.1)	0.1 (-0.1)	0.0 (0.0)	1.05 (0.0)

4.2.1 Validity of density assumption

The results presented in the previous section were derived with the 3MDv method, which assumes that the volumes of the mixture components add up to the total volume of the mixture (i.e. Eq. 33). Since the tissue parameters are taken from scientific publications, the mass densities are known for all the investigated tissues. This allows an investigation of the validity of the volume preservation assumption. The three-material decomposition method using *tabulated* mass densities as input will in the following discussion be referred to as the *3MDt* method. The method using the volume preservation assumption is as before denoted *3MDv*.

When the compositions of soft tissues were extracted using the 3MDt method, the changes compared to the results of the 3MDv method were in general within ±2 pp for the tissues yielding non-negative elemental compositions (i.e. the tissues listed in Table 3).

The extracted compositions using the 3MDt method showed a slightly lesser error for most tissues. As for instance "soft tissue", for which the error in carbon content was 12.0 pp (12.6 pp using 3MDv) and in oxygen -12.7 pp (-13.8 pp using 3MDv). The 3MDt method also managed to extract non-negative elemental compositions for more tissues.

One tissue where the volume preservation assumption is clearly not valid is inflated lung, with $\rho = 0.26\,\mathrm{g/cm^3}$. Since ρ of water, lipid and protein have values from $1.00\,\mathrm{g/cm^3}$ to $1.35\,\mathrm{g/cm^3}$, ρ of inflated lung cannot be expressed without any negative w_{base} value. Results of the 3MDv method showed a negative protein mass fraction:

$$w_{water} = 13.2, \quad w_{lipid} = 9.8, \quad w_{protein} = -22.0$$

The results of the 3MDt method were less negative, but still not acceptable;

$$w_{water} = 1.0, \quad w_{lipid} = -0.1, \quad w_{protein} = 0.1$$

The negative lipid weight resulted in a negative carbon weight (-3%), which was probably due to an inappropriate set of base materials.

Inflated lung was also investigated with the 2MD method, where the density is treated as a free parameter. The results, using deflated lung tissue and air as base materials, were:

$$w_{lung} = 1.0,\ w_{air} = -0.0,\ \rho = 0.26 \tag{47}$$

The negative value for air was only -3×10^{-5} and did not give any substantial contribution to the elemental composition of the tissue. The extracted elemental composition and mass density using the 2MD method matched tabulated values. The elemental composition for dry air was taken from the National Institute of Standards and Technology [45]: $\rho = 0.00120479\,\mathrm{g/cm^3}$, $w_C = 0.00124$, $w_N = 0.755267$, $w_O = 0.231781$, $w_{Ar} = 0.012827$.

For skeletal tissues, the volume preservation assumption did not contribute with any substantial error in the resulting elemental compositions. When compositions were extracted using the 3MDt method, the resulting elemental compositions were within ±1 pp compared to the results extracted with the 3MDv method. However, positive elemental

compositions could be extracted for practically all 19 skeletal tissues, except for cartilage, femur (30 year old) and femur (90 year old). The most negative elemental weight for these three was -0.06% (sodium content in cartilage).

The investigation using the true densities indicates that the decomposition method could be optimized with a better method to determine mass densities. The density assumption (Eq. 33) is not suitable when the tissue density is clearly different from the densities of the base materials.

5 Experiments

The purpose of the following experiments is to investigate the effect of the extracted compositions on the distributions of absorbed dose. Monte Carlo calculations of absorbed dose were performed in situations relevant for brachytherapy and heavy charged particle therapy.

5.1 Experiment 1: Brachytherapy with ^{192}Ir

5.1.1 Methods

At the University Hospital in Linköping, high dose-rate therapy of prostate cancer is performed with ^{192}Ir, an isotope that undergoes β -decay followed by emission of γ-photons. Practically all β-particles are absorbed in the capsule of the source, making the therapeutic effect attributable to the relatively high-energetic γ-photons and the characteristic X-rays.

A simulation model was set up based on a clinical treatment plan. The plan defined the planning target volume (PTV) as well as the positions and corresponding irradiation times of the source. There were in total 69 source positions with irradiation times up to 11 seconds per position.

The simulation was performed with the penmain program of the Monte Carlo code PENELOPE-2008 [46]. A phase-space file, describing the initial parameters of 10^7 photons, was generated by a user-written program. To reduce statistical uncertainties, each particle defined by the phase-space file was split into 10 equivalent particles with the parameter IPSPLI in the input file.

Initial energies of the emitted photons were sampled from corresponding yield according to the decay data for ^{192}Ir taken from the National Nuclear Data Center (NNDC), Brookhaven National Laboratory [47]. The energies and yields used are listed in Table 11. The number of photons emitted from each source position was sampled according to irradiation times, using the UNU.RAN package in the program ROOT [48]. All photons were emitted isotropically from point sources, ignoring any anisotropic effects that are caused by the applicator.

The geometry consisted of a sphere (10 cm radius) and a spherical shell (from 10 to 100 cm from origin). The cut-off energies in the sphere were set to 1 keV for photons and 100 keV for electrons. In the shell the cut-offs were set to 10 keV for photons and 1 MeV for electrons, which was above the highest energy of the emitted photons. This prevented

Table 11: Photon energies and corresponding yields for ^{192}Ir.

Energy (keV)	Yield (part./decay)	Energy (keV)	Yield (part./decay)
201.3	4.73×10^{-3}	316.5	8.27×10^{-1}
205.8	3.34×10^{-2}	416.5	6.69×10^{-3}
374.5	7.26×10^{-3}	468.1	4.78×10^{-1}
484.6	3.19×10^{-2}	612.5	5.34×10^{-3}
489.1	4.38×10^{-3}	884.5	2.91×10^{-3}
63.0	2.09×10^{-2}	66.8	4.55×10^{-2}
296.0	2.87×10^{-1}	65.1	2.66×10^{-2}
308.5	2.97×10^{-1}	75.7	1.97×10^{-2}

Table 12: Comparison between the prostate composition taken from Woodard and White [39] and composition extracted with the 3MDv method. The last row lists the differences in elemental compositions in percentage points (pp); $w^{el}_{tabulated} - w^{el}_{DECT}$.

		w_i^{el}(% by mass)							
Tissue	ρ/ [gcm^3]	H	C	N	O	Na	S	P	K
Prostate (tab.)	1.04	10.5	8.9	2.5	77.4	0.2	0.2	0.1	0.2
Prostate (3MDv)	1.04	10.6	2.2	2.1	84.9	0.0	0.1	0.0	0.0
Difference (pp)	0.0	-0.1	6.7	0.4	-7.5	0.2	0.1	0.1	0.2

electron transport in the shell, which helped to reduce the simulation times. A particle with kinetic energy below the cut-off energy is killed and the energy is locally absorbed.

An array of 25×25×19 scoring voxels for absorbed dose was centered at the origin of the sphere; each voxel with volume 0.25x0.25x0.25 cm^3. The scoring voxels belonging to the PTV was sorted out by a mask, see Figures 11a and 11b.

This set-up was used to investigate distributions of absorbed dose in ^{192}Ir brachytherapy for five different materials:

1. prostate tissue with tabulated elemental composition
2. prostate tissue with an elemental composition extracted with the 3MDv method
3. water
4. prostate tissue with 2% calcifications by weight
5. prostate tissue with 5% calcifications by weight

Table 12 shows a comparison of the tabulated and the extracted prostate compositions. The elemental compositions of the calcified prostate tissues can be seen in Table 1.

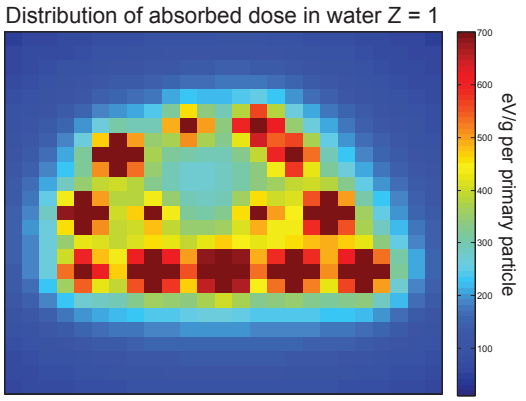

(a) A sectional view of the three-dimensional distribution of absorbed dose in water. The high-dose regions coincide with positions of the source.

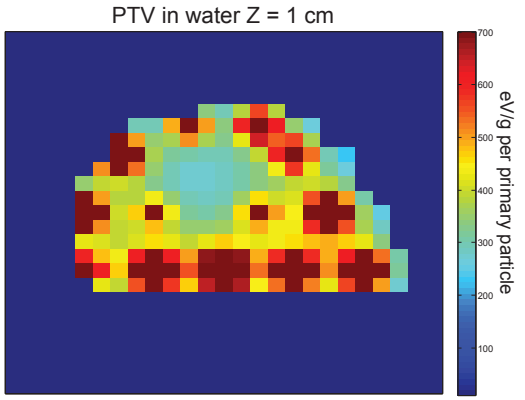

(b) A sectional view of the distribution of absorbed dose in volume corresponding to PTV. The values of absorbed dose in voxels outside the PTV are set to zero.

Figure 11

Dose volume histograms (DVHs) were constructed with a MATLAB [44] script to evaluate the simulation results. These histograms are commonly used in clinics for comparison and evaluation of different treatment plans.

Appendix C contains a PENELOPE input file for the ^{192}Ir simulation and Appendix D contains the MATLAB script used to plot DVHs.

5.1.2 Results and discussion

Figure 12 shows DVHs for ^{192}Ir brachytherapy in (i) water, (ii) prostate tissue of tabulated elemental composition and (iii) extracted prostate composition. The DVHs for the three tissues are practically indistinguishable, indicating that the prostate compositions are dosimetrically equivalent to water at the considered photon energies. The long tails seen in the DVHs are due to the use of point sources. Voxels that contain a source will receive a high absorbed dose, which in reality would have been deposited in the source capsule.

Figure 13 shows DVHs for prostate tissues with 2% and 5% calcifications. Even though the calcifications increase the effective atomic number of the tissues (the 5% calcified prostate contains almost 2% calcium, $Z = 20$)) the absorbed dose distributions were similar to the non-calcified tissue. This is probably due to the relatively high energies of the photons emitted in the decay of ^{192}Ir, the mean energy is approximately 370 keV. According to the NIST cross-section database [49] incoherent scatter stands for 99.5% of the total photon attenuation in the 5% calcified prostate (at 370 keV). Photoelectric effect stands for only 0.0007%, and coherent scatter for the remaining part, almost 0.5%. The cross-section for incoherent scatter is proportional to the electron density and relatively independent of the atomic number. The changes in elemental compositions were therefore not enough to give any observable impact to the absorbed dose distributions.

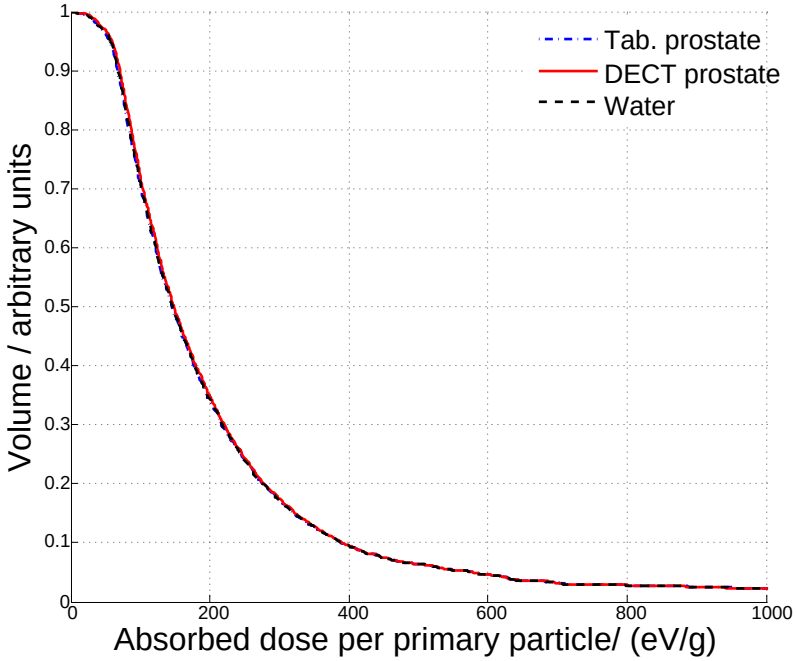

Figure 12: Dose-volume histograms for ^{192}Ir simulations with water, tabulated prostate tissue and prostate tissue with extracted composition.

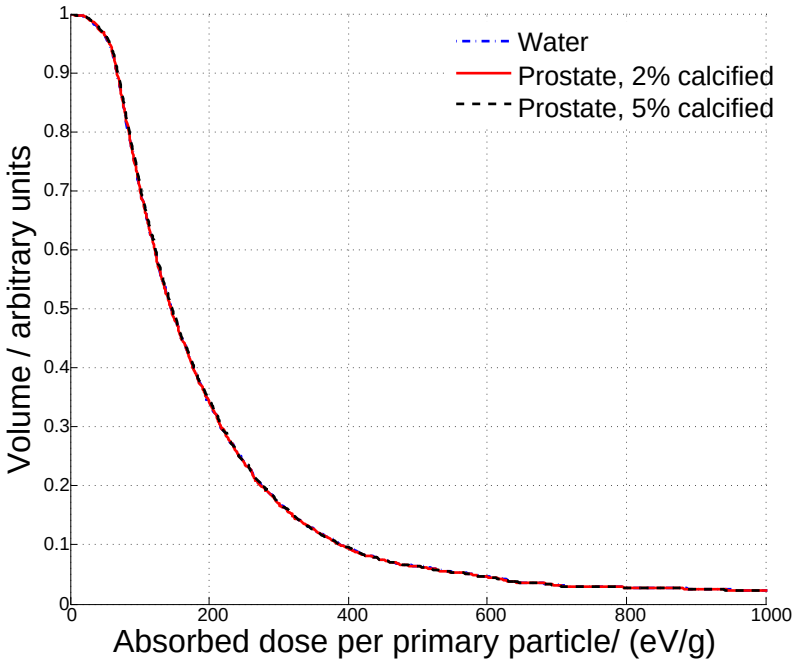

Figure 13: Dose-volume histograms for ^{192}Ir simulations with water and prostate tissue with 2% and 5% calcifications by mass.

The calcifications were in these simulations distributed homogeneously in the prostate. In reality the calcifications appear as solid grains in clusters or as larger stones [41]. These highly attenuating structures will cause complicated scattering and shielding effects that will affect the absorbed dose distribution. A more realistic geometry could be achieved by randomly spreading calcifications of various sizes as clusters in the prostate volume.

5.2 Experiment 2: Brachytherapy with ^{125}I

Since no effects in absorbed dose could be observed in Experiment 1, further simulations were performed with lower photon energies. In Experiment 2 the isotope ^{125}I was used, which is commonly used for low-dose rate brachytherapy of prostate cancer.

5.2.1 Methods

Monte Carlo dose calculations were performed with the program penmain of the Monte Carlo code PENELOPE. No clinical treatment plan could be obtained for ^{125}I therapy. Instead, a simulation geometry was used with a single point source in a homogeneous sphere. The energy spectrum used in the simulations was taken from NNDC [47], Table 13. Conversion electrons and Auger electrons that are emitted in the decay of ^{125}I were assumed to be totally absorbed in the capsule of the source. All photons were emitted isotropically from the source.

Cut-off energies were set to 10 keV for electrons and 1 keV for photons. Enough particles were simulated to reach a relative expanded uncertainty arising from random effects below 2.3% at the confidence level of 99.7% (coverage factor k=3) for the absorbed dose in all shells.

The sphere surrounding the radiation source was divided in several spherical shells with thicknesses of 0.5 mm. Each shell registered the energy imparted, which was converted to average absorbed dose per primary particle. The absorbed dose values were multiplied with the square of the radius to eliminate the inverse square dependence.

The same five materials were investigated as in Experiment 1: (i) tabulated prostate tissue composition, (ii) prostate composition extracted with the 3MDv method, (iii) water, (iv) prostate tissue with 2% calcifications and (v) prostate tissue with 5% calcifications.

Appendix E contains a PENELOPE input file for the ^{125}I simulations.

Table 13: Photon energy spectrum with corresponding yields for ^{125}I .

Energy (keV)	Yield (part./decay)
35.49	6.68×10^{-2}
27.47	7.44×10^{-1}
27.20	4.00×10^{-1}
31.00	2.60×10^{-1}
3.77	1.49×10^{-1}

5.2.2 Results and discussion

Figure 14a shows the absorbed dose relative to water as a function of radius in the prostate tissue of tabulated and extracted composition. Close to the source, the absorbed dose relative to water was near unity for both concerned tissues. Farther from the source, the dose decreased with increasing distance. The dose to the extracted tissue composition followed the same trend as the tabulated, but consistently underestimated the dose slightly. The mass densities of the tissues were identical ($\rho = 1.04$ g/cm^3) so the differences in depth-doses were due to variations in the elemental compositions. The carbon content in the 3MDv-tissue was underestimated with -6.7 pp, and the oxygen content overestimated with 7.5 pp. As discussed in Section 4.2, the reason for this may be that the tabulated prostate tissue contained phosphorus and potassium ($w_{\mathrm{P}} = 0.1\%$ and $w_{\mathrm{K}} = 0.2\%$) which were not present in the base materials.

Figure 14b shows a similar plot for prostate tissues with 2% and 5% calcifications. Though any effects of the calcifications could not be seen in the dose distributions in Experiment 1, the effects were substantial at the low photon energies emitted by ^{125}I (mean energy approximately 28 keV). At 1 mm distance from the point source, the absorbed dose to the 5% calcified prostate tissue was 49.7% higher than that to water. In the 2% calcified tissue the absorbed dose was at most 21.5% higher than in water. The higher doses were attributable to the larger photoelectric cross-section at these lower energies. Photoelectric effect is heavily dependent on atomic number. Therefore at these energies, any changes in elemental composition may considerably change the attenuating properties. In the 5% calcified prostate, photoelectric effect stands for 54.4% of the total attenuation for 28 keV photons, according to the NIST cross-section database [49]. The corresponding value for the average photon energy emitted by ^{192}Ir was 0.0007%.

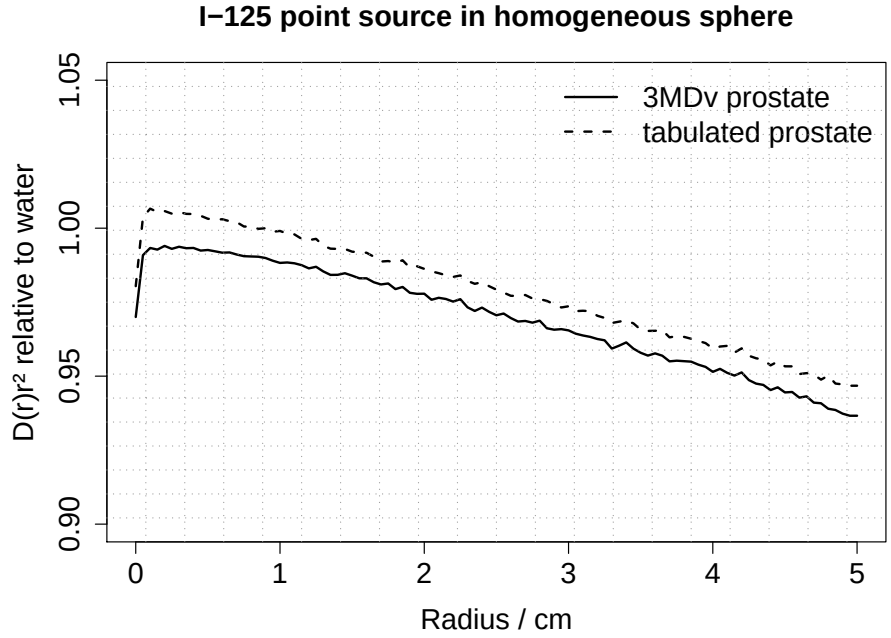

(a) Prostate tissues with tabulated elemental composition, and with composition extracted with the 3MDv method.

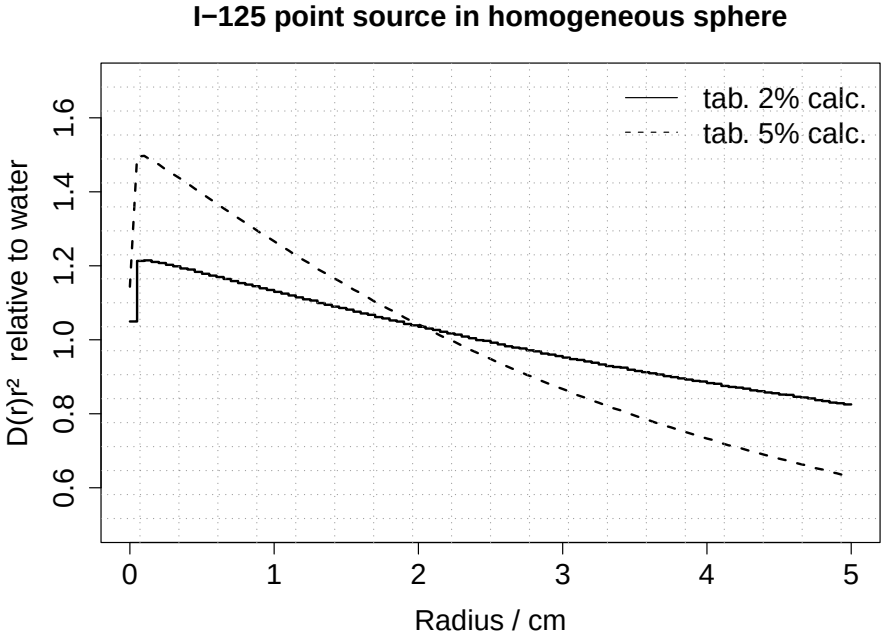

(b) Prostate tissues with 2% and 5% of calcifications.

Figure 14: Absorbed dose relative to water as a function of radius. The value of absorbed dose is multiplied with the square of the radius to compensate for the inverse square dependence on the fluence.

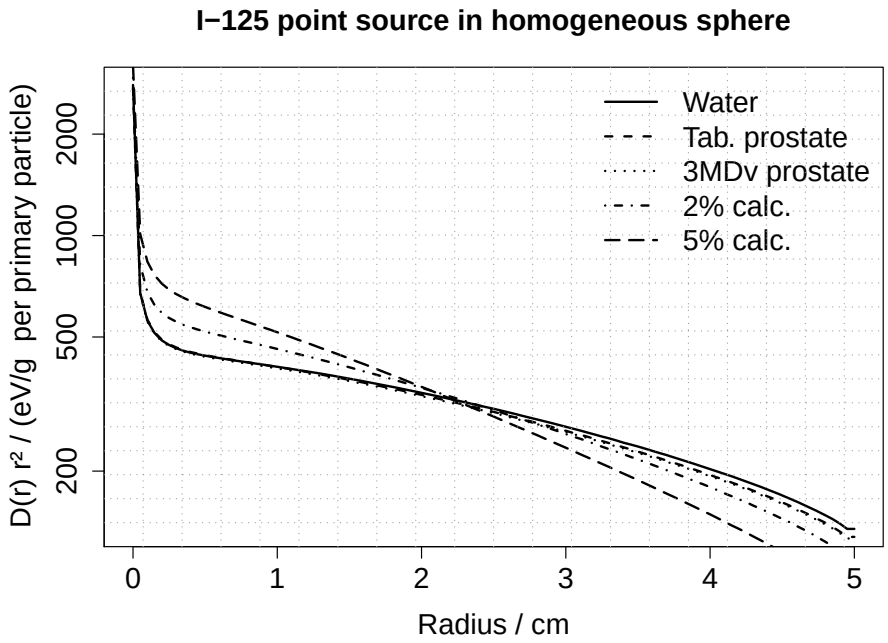

Figure 15: Absorbed dose as a function of radius in water, prostate with tabulated composition, extracted prostate composition, 2% calcified prostate and 5% calcified prostate tissue. The doses are corrected for the inverse square dependence. Note the logarithmic y-scale.

Differences in absorbed dose could also be seen at relatively large distance from the source. At 5 cm, the absorbed dose to 5% calcified prostate was 36.6% lower than for water, and the dose to the 2% calcified prostate was 17.5% lower than for water. However, as shown in Figure 15, the absorbed doses at 5 cm distance were only in the order of percent of the highest values. The errors in absorbed dose at this distance were therefore of minor relevance.

5.3 Experiment 3: Proton and ^{12}C-ion therapy

5.3.1 Methods

Monte Carlo dose calculations were performed with the code FLUKA [50, 51] to investigate the extracted tissue compositions in proton and carbon ion therapy. A cylinder of radius 100 cm was irradiated with monoenergetic pencil beams of different particles. The target cylinder was set-up based on an abdominal CT image and consisted of several sections, or slabs, corresponding to different tissue types. The CT image was taken from the master thesis report of Evelina Olofsson [52] and is shown in Figure 16. Three beam angles were simulated: front, oblique and side. The beam angles were defined in the work of Olofsson and were not chosen because of the correspondence with any therapeutic situation.

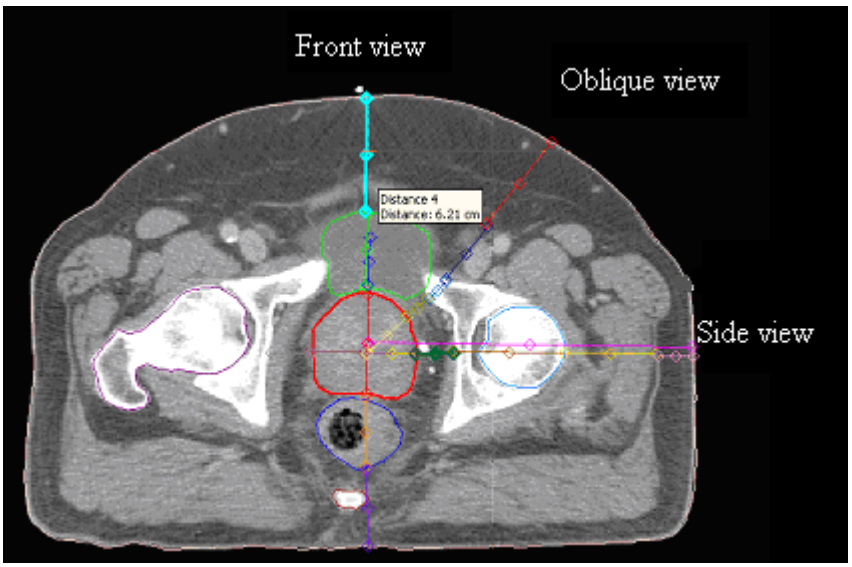

Figure 16: The abdominal CT image that served as a base for the simulation geometry. Image courtesy of Anders Ahnesjö. Originally from the master thesis of Olofsson [52].

Three multislab cylinders of radius 100 cm were constructed, similar to the schematic image shown in Figure 17. The tissues used and the thicknesses of each cylinder slab are presented in Table 14.

The multislab geometries were evaluated for three different materials:

1. tabulated elemental compositions
2. elemental compositions derived with the 3MDv method
3. water slabs with the same electron density as the tabulated elemental compositions

To extract tissue compositions with the 3MDv method, μ-values were taken at the fluence weighted mean energies of the 80 kV and tin-filtered 140 kV spectra. The elemental compositions for soft tissues were derived with the base materials lipid, protein and water. As shown in the scatter plot in Figure 18a, adipose tissue and "soft tissue" lied inside the triangle confined by the base materials. GI-tract, prostate and skeletal muscle were slightly outside, indicating that at least one weight fraction would be negative. This was confirmed by the results that revealed negative lipid weights for skeletal muscle ($w_{lipid} = -9\%$), adipose ($w_{lipid} = -0.5\%$) and prostate ($w_{lipid} = -5.8\%$). When elemental compositions were derived, the positive contributions from water and protein outweighed the contributions from the slightly negative lipid values. The resulting elemental compositions were all non-negative, meaning that they could be used in the Monte Carlo simulations.

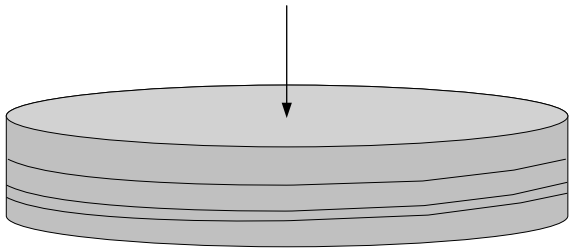

Figure 17: Schematic image of the experimental set-up used in the heavy charged particle simulations.

Table 14: Dimensions of the cylinders used in the FLUKA simulations. The views refer to the different angles of incidence marked in Figure 16. All tissue compositions were taken from articles by Woodard and White (1986) [39] and White et al (1987) [40]. When compositions were available for both sexes, male tissues were chosen.

(a)

Front view	
Tissue	Thickness / cm
Adipose 2	6.2
Soft	4.0
Prostate	5.5
GI tract. small intestine	3.8
Soft	10.5

(b)

Side view	
Tissue	Thickness / cm
Skeletal muscle 2	6.9
Innominate bone	6.1
Soft	2.1
Prostate	5.8
Soft	2.2
Innominate bone	6.9

(c)

Oblique view	
Tissue	Thickness / cm
Adipose 2	5.8
Skeletal muscle 2	3.6
Bone	1.3
Soft	1.5
Prostate	6.0

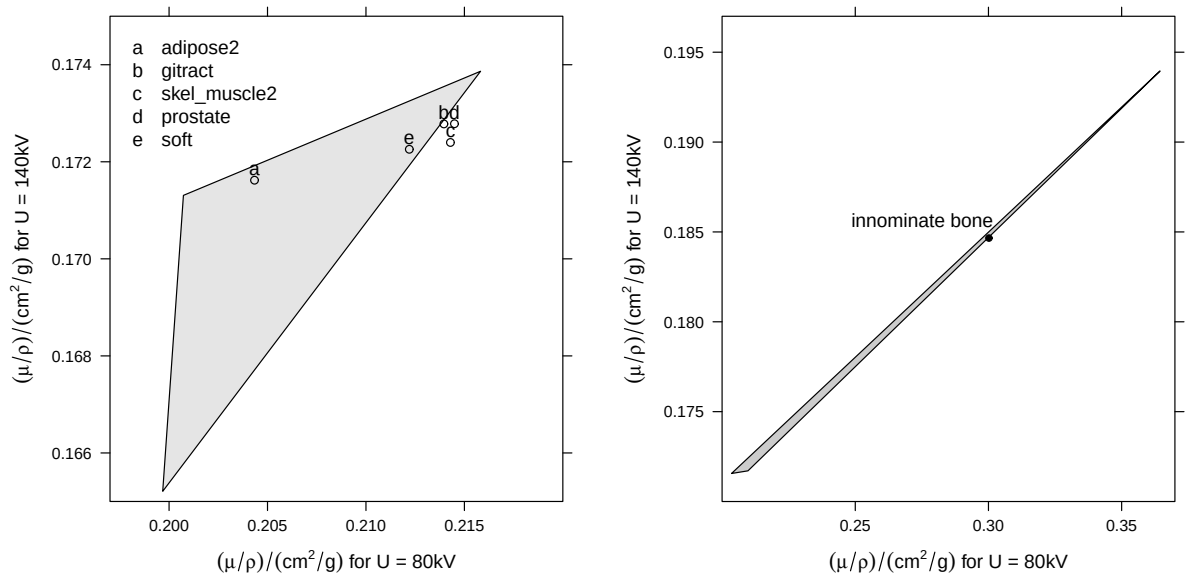

(a) (b)

Figure 18: Scatter plots of mass attenuation coefficients showing (a) the soft tissues and (b) the skeletal tissue used in the multislab simulations.

To extract the elemental compositions of innominate bone, the base materials red marrow, yellow marrow and cortical bone were used, Figure 18b. The 3MDv method resulted in positive values for all base material proportions and thus also a positive elemental composition. The tissue compositions derived with the 3MDv-method are presented in Table 15.

Besides the tabulated and the extracted tissue parameters, simulations were also performed with water of different mass densities. The same cylindrical geometry was used as in the other simulations. The mass densities of the different water slabs were modified to reach the same electron densities as the tabulated tissues corresponding to the same slab. The purpose was to reproduce the ideal response of a single energy CT scanner, which can be used to extract spatial distributions of electron densities. The electron densities were calculated as:

$$\rho_e = \mathrm{N_A} \sum_i \frac{w_i Z_i}{M_i} \tag{48}$$

Where $\mathrm{N_A}$ is the Avogadro constant and w_i, Z_i, M_i the mass fraction, atomic number and molar mass of element i. The water slabs were only evaluated with irradiation from the side.

Each of the three multislab phantoms, corresponding to irradiation from different beam angles, were evaluated with both protons and ^{12}C-ions. The beam energies, Table 16, were chosen to position the Bragg peak inside the prostate volume.

Table 15: The extracted elemental compositions for the tissues used in heavy charged particle simulations.

	w_i^{el} (% by mass)						
Tissue	H	C	N	O	S	Other elements	ρ / $\left(\mathrm{g \cdot cm^{-3}}\right)$
Adipose2	11.5	57.1	0.6	30.9	-	-	0.95
Soft	10.6	13	2.2	74.0	0.1	-	1.03
Skeletal muscle2	10.5	0.7	2.4	86.2	0.1	-	1.05
Prostate	10.6	2.2	2.1	84.9	0.1	-	1.04
GI tract. small intestine	10.7	5.3	1.8	82.1	0.1	-	1.03
Innominate bone (male)	6.4	28.2	3.6	41.7	0.2	S(0.2), Cl(0.1), P(6.1) K(0.1), Ca(13.3)	1.41

Table 16: Kinetic energy per unit mass for the particles used for the different beams.

	Energy / (MeV/u)		
Particles \ Beam view	Front	Oblique	Side
Protons	135	150	170
^{12}C-ions	250	285	340

For the proton simulations, 25 runs of 10^6 particles each were performed and for the ^{12}C-ion simulations 25 runs of 25000 particles each. The ^{12}C-ion experiments were run with the relativistic quantum molecular dynamics model (rQMD 2.4) to account for nuclear interactions. The proton beam experiments were performed using the default model. Appendix F contains a FLUKA input file for a proton simulation.

5.3.2 Results and discussion

The resulting depth-dose curves and lateral dose spread for protons in the side view are presented in Figures 19 - 21, and for ^{12}C-ions in Figures 22 - 24.

The errors in Bragg peak position for the extracted tissue compositions were less than 0.3 mm, both for protons and ^{12}C ions. The water slabs with the same ρ_e as the tabulated tissues had an offset in Bragg peak position of approximately 1.2 mm for protons and approximately 1.6 mm for ^{12}C ions.

Figures 21 and 24 show the lateral spread of the two different particle beams. The absorbed dose sharply decreased with distance from the beam axis, especially for the heavier ^{12}C-ions. No significant difference could be seen for the three different materials investigated.

The resulting absorbed dose distributions for the front and oblique view were similar to the side view; the errors in Bragg peak position for the extracted tissues were below 0.3 mm in all cases.

The patient geometry used in the simulations was represented with a few homogeneous

slabs. This approach did not take into account the variations in structure and composition that is seen for real patients. Even though the simulations contained several simplifications the results indicated that the extracted tissue compositions were similar to the tabulated tissues regarding distributions of absorbed dose.

The simulations with water slabs, representing an ideal single energy CT approach, were not considerably worse than for the 3MDv extracted tissues. However, to achieve submillimeter accuracy elemental compositions may need to be taken into account.

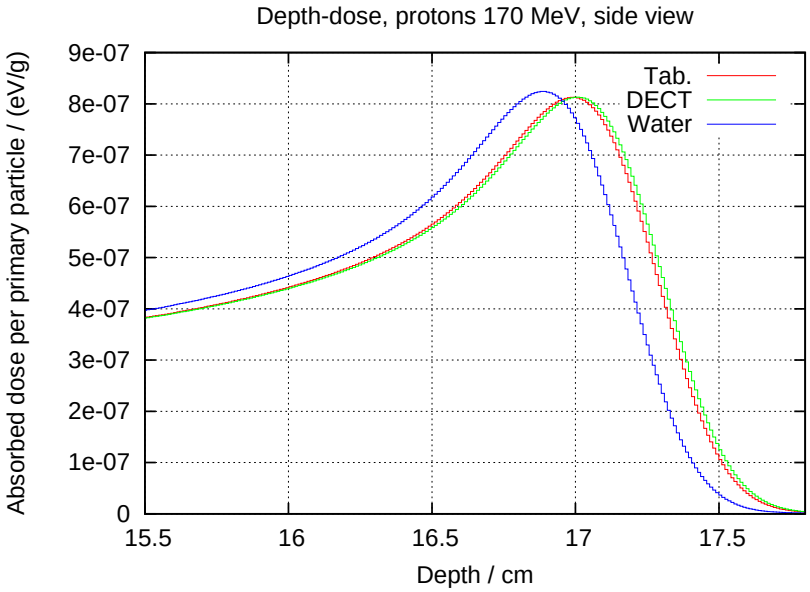

Figure 19: Absorbed dose as a function of depth for the proton beam incident from the side. "DECT" refers to the tissue compositions derived with the 3MDv method.

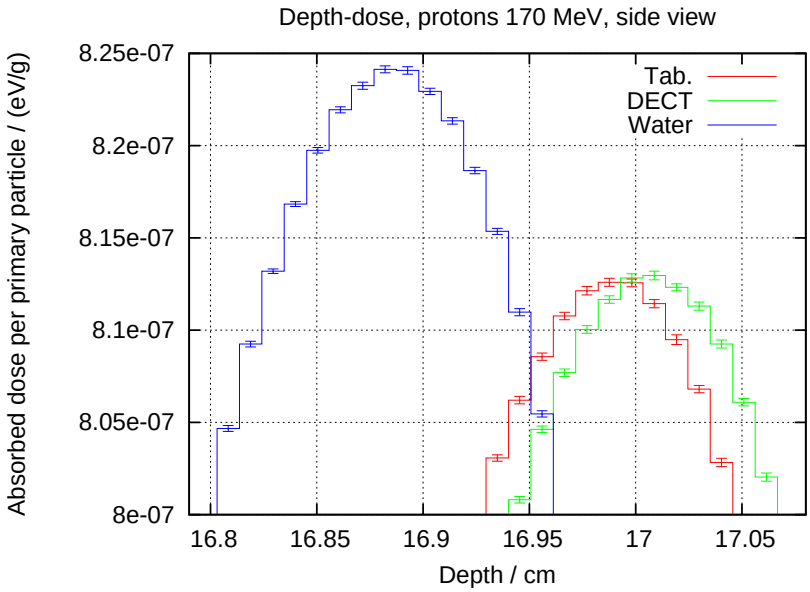

Figure 20: Close-up on the Bragg peak for the protons beams incident from the side. The error bars represent the standard uncertainty arising from random effects.

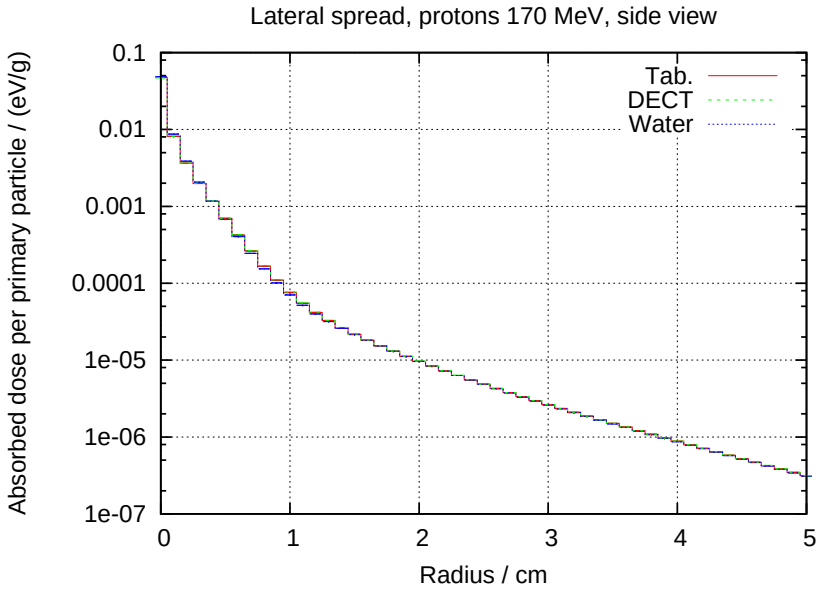

Figure 21: Lateral dose distribution for the proton beam incident from the side.

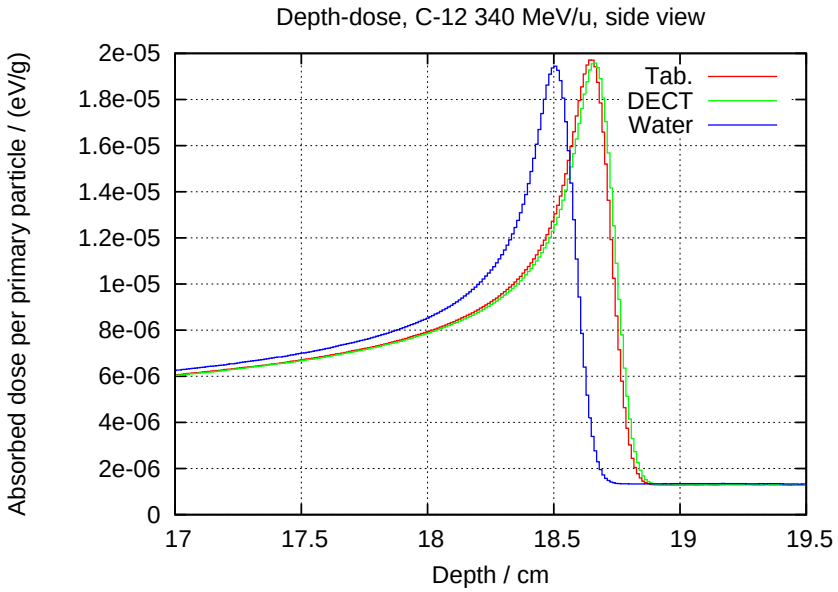

Figure 22: Absorbed dose as a function of depth for the ^{12}C-ion beams incident from the side. "DECT" refers to the tissue compositions derived with the 3MDv method.

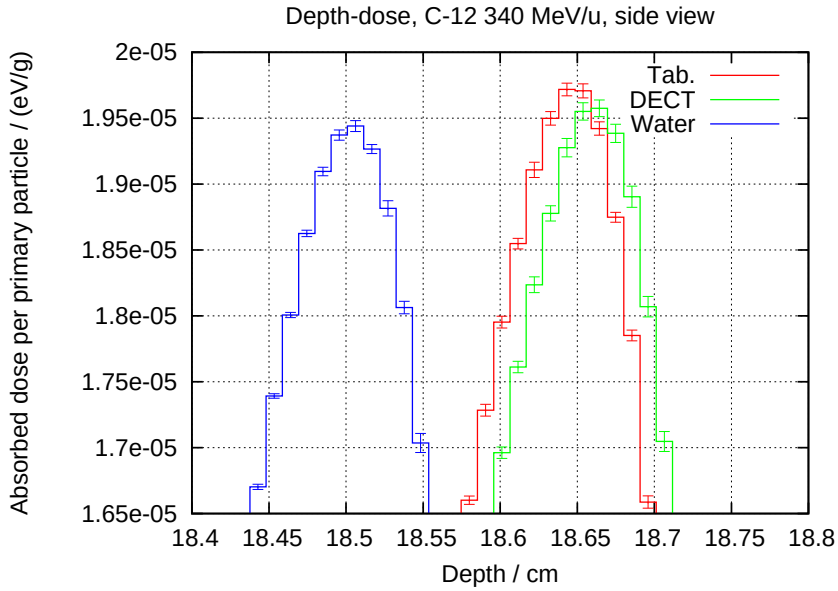

Figure 23: Close-up on the Bragg peak of the ^{12}C-ion beams incident from the side. The error bars represent the standard uncertainty arising from random effects.

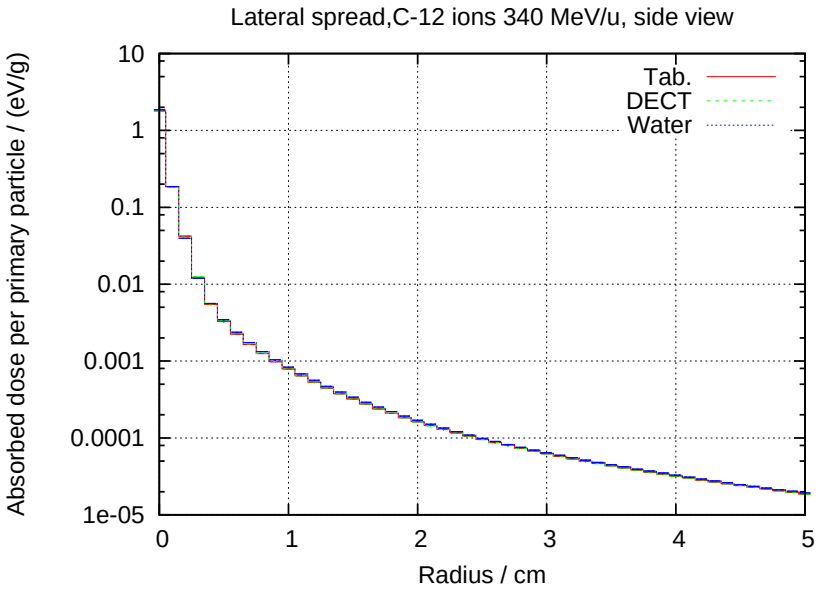

Figure 24: Lateral dose distributions for the ^{12}C-ion beams incident from the side.

6 Summary

To be able to describe the elemental composition of a material, some issues need to be overcome. First, a set of relevant base materials need to be chosen. This was shown to significantly affect the accuracy of the derived elemental compositions. For instance, several soft tissues could be described with both the base materials used to decompose skeletal tissues as well as soft tissues. However, the resulting compositions had large errors when an inappropriate base material set was applied. Therefore, any indications or expectations on the compositions of a tissue may be beneficial for the decomposition methods. As mentioned before, more work of finding suitable base materials can potentially lead to better decomposition results.

The decomposition was done with the simulated response of a DECT scanner, solely based on the linear attenuation coefficients at the effective energy of the calculated photon spectra. However, CT image artifacts caused by beam hardening, scattered radiation and quantum noise may affect the decomposition results. Clavijo et al. 2009 [11] and Liu et al. 2009 [16] have reported results from a decomposition method similar to the 3MDv-method (cf. Section 3.1.5). They found that scattering artifacts in the CT data decrease the accuracy of the decomposition result. In view of these results it would be of interest to investigate how scattering affects our algorithms. However, this was not in the scope for the current work. A CT phantom constructed with materials of known compositions could be used to assess the performance of commercial beam hardening and scatter artifact corrections, which are implemented in modern CT scanners. This would give an opportunity to investigate the decomposition methods in real conditions.

The investigated three-material decomposition methods used the assumption of density preservation. Since the true densities were known, the validity of the density assumption could be analyzed (cf. Section 4.2.1). For the tissues and base materials used, a slight improvement could be seen in the accuracy of the resulting compositions. Liu et al. [16] also recognised the potential weakness of the density assumption in three-material decomposition. They proposed an interesting solution to this. By first performing a parameterization of μ into contributions from photoelectric effect and incoherent scattering they derived the effective atomic number and effective mass density of a volume of interest (i.e. the approach originally suggested by Alvarez et al. [4]). The effective mass density was then used as input to a decomposition model similar to 3MDv (cf. 3.1.6). This approach has not been evaluated in this work, but could potentially be of benefit in situations where the density approach is not valid.

The derived elemental compositions were evaluated with Monte Carlo simulations to investigate the effect on absorbed dose distributions. This was done for prostate treatments with heavy charged particles and brachytherapy. These two radiation treatment types are expected to benefit from information of tissue compositions. For MV photon therapy, the need of information about atomic numbers may be of minor importance. Incoherent scattering and pair production are the dominating interaction processes for high-energetic photons, for which the cross-sections do not depend on atomic numbers as strongly as photoelectric effect does. This was seen in the ^{192}Ir brachytherapy simulation (cf. Section 5.1),

where the mean photon energy were approximately 370 keV. The qualitative evaluation of dose volume histograms could not resolve any substantial difference between the investigated tissue compositions. Yet, the tissue decomposition algorithms should be evaluated also for MV photon therapy, but it was not the focus for the current work.

Results from Monte Carlo simulations of particle transport reflect the physical models and approximations used and should not uncritically be considered as the truth. Both Monte Carlo code systems used in this work, FLUKA and PENELOPE, are well benchmarked with other models and experimental data [53, 54]. FLUKA is used at the Heidelberg Ion Therapy Center (HIT) to validate the analytical treatment planning system [55]. It would be of interest to investigate the how the derived tissue compositions affects the results of commercial treatment planning systems.

7 Conclusions

A three-material decomposition method in DECT has been investigated for a wide range of tissue compositions. Elemental compositions could be derived for skeletal tissues with the largest error in elemental weight of 3.0 percentage points. However, the selected base materials for soft tissues for were not suitable in all cases. Decomposition into water, lipid and protein gave errors up to 19.2 percentage points. Investigations of appropriate base materials are needed to improve the results for soft as well as skeletal tissues.

The investigated method assumes that the mass density of the tissue can be expressed with the mass densities of the base materials. This approach has shown not to be suitable when the density of the tissue clearly is deviating from that of the base materials. A more sophisticated way to extract the mass density may improve the method.

A method to extract elemental compositions of tissues could be of benefit for several medical applications. The focus of this study was on radiation treatment planning for brachytherapy and therapy with heavy charged particles.

While brachytherapy with ^{192}Ir was shown not to be very sensitive to differences in elemental compositions, the impact in ^{125}I brachytherapy was substantial, especially when the prostate tissue contained calcifications. The possibility to map out and extract compositional data of such heterogeneities could help to improve the accuracy of brachytherapy.

The extracted tissue compositions introduced an error to the Bragg peak positions for proton and carbon ion therapy with at most 0.3 mm. These relatively accurate results indicate that the decomposition method could help to reduce the treatment margins around the target volume, hence contributing to a better treatment.

However, this early study has been performed under several simplifications. Various factors that may affect the performance and accuracy in reality have not been accounted for. Further studies are required to analyze the effects of, among other, individual variations in tissue compositions and CT artifacts as beam hardening, scatter and patient movements.

Acknowledgments

I would like to express my sincere gratitude to everyone involved in this project.

- My supervisor Alexandr Malusek for all the valuable support and feed-back and for introducing me to a lot of useful computer software
- My supervisor Gudrun Alm Carlsson for support and encouragement
- Arif Muhammad for inspirational discussions and for valuable help with programming issues
- Maria Magnusson-Seger for teaching me about computed tomography and reconstruction algorithms

Finally a thank you to everyone at Medical Radiation Physics at Linköping University for making it such a nice place.

References

[1] Peter Metcalf, Tomas Kron, and Peter Hoban. *The Physics of Radiotherapy X-rays and Electrons*. Medical Physics Publishing, 2007.

[2] Avinash C. Kak and Malcolm Slaney. *Principles of Computerized Tomographic Imaging*. IEEE Press, Philadelphia, PA, USA, 1999.

[3] Michael R. Millner, William D. McDavid, Robert G. Waggener, Michael J. Dennis, William H. Payne, and Victor J. Sank. Extraction of information from CT scans at different energies. *Medical Physics*, 6(1):70–71, 1979.

[4] R E Alvarez and A Macovski. Energy-selective reconstructions in X-ray computerised tomography. *Physics in Medicine and Biology*, 21(5):733–744, 1976.

[5] Thorsten R. C. Johnson, Bernhard Krauss, Martin Sedlmair, Michael Grasruck, Herbert Bruder, Dominik Morhard, Christian Fink, Sabine Weckbach, Miriam Lenhard, Bernhard Schmidt, Thomas Flohr, Maximilian F. Reiser, and Christoph R. Becker. Material differentiation by dual energy CT: Initial experience. *European Radiology*, 17(6):1510–1517, 2007.

[6] E.B. Podgorsak. *Radiation Oncology Physics: A Handbook for Teachers and Students*. International Atomic Energy Agency, 2005.

[7] T. Knöös, M. Nilsson, and L. Ahlgren. A method for conversion of hounsfield number to electron density and prediction of macroscopic pair production cross-sections. *Radiotherapy and Oncology*, 5(4):337–345, 1986.

[8] Hongyu Jiang, Joao Seco, and Harald Paganetti. Effects of Hounsfield number conversion on CT based proton monte carlo dose calculations. *Medical Physics*, 34(4):1439–1450, 2007.

[9] Guillaume Landry, Brigitte Reniers, Lars Murrer, Ludy Lutgens, Esther Bloemen-Van Gurp, Jean-Philippe Pignol, Brian Keller, Luc Beaulieu, and Frank Verhaegen. Sensitivity of low energy brachytherapy monte carlo dose calculations to uncertainties in human tissue composition. *Medical Physics*, 37(10):5188–5198, 2010.

[10] Anno Graser, Thorsten Johnson, Hersh Chandarana, and Michael Macari. Dual energy CT: preliminary observations and potential clinical applications in the abdomen. *European Radiology*, 19:13–23, 2009.

[11] Carolina Arboleda Clavijo and Norbert J. Pelc. Image-quality optimization for dual energy computed tomography (DECT) three-material decomposition. *Revista Ingenieria Biomedica*, 3:33–42, 2009.

[12] Magdalena Bazalova, Jean-Francois Carrier, Luc Beaulieu, and Frank Verhaegen. Dual-energy CT-based material extraction for tissue segmentation in Monte Carlo dose calculations. *Physics in Medicine and Biology*, 53(9):2439–2456, 2008.

[13] Uwe Schneider, Pedroni Eros, and Lomax Antony. The calibration of CT Hounsfield units for radiotherapy treatment planning. *Physics in Medicine and Biology*, 41(1):111–124, 1996.

[14] Frank Verhaegen and Slobodan Devic. Sensitivity study for CT image use in Monte Carlo treatment planning. *Physics in Medicine and Biology*, 50(5):937–946, 2005.

[15] Wilfried Schneider, Thomas Bortfeld, and Wolfgang Schlegel. Correlation between CT numbers and tissue parameters needed for Monte Carlo simulations of clinical dose distributions. *Physics in Medicine and Biology*, 45(2):459–478, 2000.

[16] Xin Liu, Lifeng Yu, and Andrew N. Primak. Quantitative imaging of element composition and mass fraction using dual-energy CT: Three-material decomposition. *Medical Physics*, 36(5):1602–1610, 2009.

[17] Aaron So, Jiang Hsieh, Jian-Ying Li, and Ting-Yim Lee. Beam hardening correction in ct myocardial perfusion measurement. *Physics in Medicine and Biology*, 54(10):3031, 2009.

[18] Frederick Kelcz, Peter M. Joseph, and Sadek K. Hilal. Noise considerations in dual energy ct scanning. *Medical Physics*, 6(5):418–425, 1979.

[19] Veronique Rebuffel and Jean-Marc Dinten. Dual-energy X-ray imaging: benefits and limits. *Insight: Non-Destructive Testing & Condition Monitoring*, 49(10):589–595, 2007.

[20] Philips Healthcare. Exploring the spectrum: Advances and potential for Spectral CT. `http://www.healthcare.philips.com/main/products/ct/products/spectral_ct/index.wpd`, 21 nov 2010.

[21] GE Healthcare, Discovery CT 750hd Gemstone. `http://www.gehealthcare.com/promo/discovery_ct750hd/overview_leadingedge_gemstone.html`, 05 dec 2010.

[22] Yiannis Kyriakou and Willi A Kalender. Intensity distribution and impact of scatter for dual-source ct. *Physics in Medicine and Biology*, 52(23):6969, 2007.

[23] Philip P. Connell and Samuel Hellman. Advances in radiotherapy and implications for the next century: A historical perspective. *Cancer Research*, 69(2):383–392, 2009.

[24] Francesca Pistis, Ferran Guedea, Joan Pera, Cristina Gutierrez, Montse Ventura, Alfredo Polo, Evelyn Martinez, Ana Boladeras, Ferran Ferrer, Pietro Gabriele, and Luis Linares. External beam radiotherapy plus high-dose-rate brachytherapy for treatment of locally advanced prostate cancer: The initial experience of the Catalan Institute of Oncology. *Brachytherapy*, 9(1):15–23, 2010.

[25] R. Nath, L. L. Anderson, G. Luxton, K. A. Weaver, J. F. Williamson, and A. S. Meigooni. Dosimetry of interstitial brachytherapy sources: Recommendations of the AAPM radiation therapy committee Task Group No. 43. *Medical Physics*, 22:209–234, 1995.

[26] M. J. Rivard, B. M. Coursey, L. A. DeWerd, W. F. Hanson, M. S. Huq, G. S. Ibbott, M. G. Mitch, R. Nath, and J. F. Williamson. Update of AAPM Task Group No. 43 Report: A revised AAPM protocol for brachytherapy dose calculations (AAPM Report No. 84). *Medical Physics*, 31:633–674, 2004.

[27] Jean-Francois Carrier, Michel D'Amours, Frank Verhaegen, Brigitte Reniers, Andre-Guy Martin, Eric Vigneault, and Luc Beaulieu. Postimplant dosimetry using a monte carlo dose calculation engine: A new clinical standard. *Int J Radiat Oncol Biol Phys*, 68(4):1190–1198, July 2007.

[28] Saverio Braccini. Scientific and Technological Development of Hadrontherapy. Number arXiv:1001.0860, Jan 2010. Presented at the 11th ICATPP Conference on Astroparticle, Particle, Space Physics, Detectors and Medical Physics Applications, Como (Italy), October 2009.

[29] Pedro Andreo. Note on the clinical spatial resolution achievable with protons and heavier charged particle radiotherapy beams. *Physics in Medicine and Biology*, 54(11):N205–N215, 2009.

[30] Andrea Mairani. *Nucleus-nucleus interaction modelling and applications in ion therapy treatment planning*. PhD thesis, University of Pavia, 2007.

[31] International Commission on Radiation Units and Measurements. Prescribing, Recording, and Reporting Proton-Beam Therapy. *ICRU Report 78*, (2), 2007.

[32] N. Reynaert, S.C. van der Marck, D.R. Schaart, W. Van der Zee, C. Van Vliet-Vroegindeweij, M. Tomsej, J. Jansen, B. Heijmen, M. Coghe, and C. De Wagter. Monte Carlo treatment planning for photon and electron beams. *Radiation Physics and Chemistry*, 76(4):643 – 686, 2007.

[33] M Yang, G Virshup, J Clayton, X R Zhu, R Mohan, and L Dong. Theoretical variance analysis of single- and dual-energy computed tomography methods for calculating proton stopping power ratios of biological tissues. *Physics in Medicine and Biology*, 55(5):1343–1362, 2010.

[34] Swedish Standards Institute. Quantities and units - Part 10: Atomic and nuclear physics (SS-ISO 80000-10:2009, IDT), 2010-01-15.

[35] D.F. Jackson and D.J. Hawkes. X-ray attenuation coefficients of elements and mixtures. *Physics Reports*, 70(3):169–233, 1981.

[36] Robley D. Evans. *The Atomic Nucleus*. Tata McGraw Hill Publishing Company Limited, 1955.

[37] International Commission on Radiation Units and Measurements. Photon, Electron, Proton and Neutron Interaction Data for Body Tissues. *ICRU Report 46*, 1992.

[38] International Commission on Radiation Units and Measurements. Tissue Substitutes in Radiation Dosimetry and Measurements. *ICRU Report 44.*, may 1988.

[39] H. Q. Woodard and D. R. White. The composition of body tissues. *Br J Radiol*, 59(708):1209–1218, 1986.

[40] D. R. White, H. Q. Woodard, and S. M. Hammond. Average soft-tissue and bone models for use in radiation dosimetry. *Br J Radiol*, 60(717):907–913, 1987.

[41] J.H. Suh, J.M. Gardner, K.H. Kee, S. Shen, A.G. Ayala, and J.Y. Ro. Calcifications in prostate and ejaculatory system: a study on 298 consecutive whole mount sections of prostate from radical prostatectomy or cystoprostatectomy specimens. *Annals of Diagnostic Pathology*, 12(3):165–170, 2008.

[42] G Poludniowski, G Landry, F DeBlois, P M Evans, and F Verhaegen. SpekCalc : A program to calculate photon spectra from tungsten anode X-ray tubes. *Physics in Medicine and Biology*, 54(19):N433, 2009.

[43] Nuclear Data Services International Atomic Energy Agency. the Evaluated Photon Data Library, '97 Version, 1997.

[44] The MathWorks Inc. MATLAB 7.9.0 (r2009b).

[45] National Institute of Standards and Technology. `http://physics.nist.gov/`.

[46] PENELOPE 2008.1. A Code System for Monte-Carlo Simulation of Electron and Photon Transport. `http://www.nea.fr/tools/abstract/detail/nea-1525/`. NEA-1525/016.

[47] Brookhaven National Laboratory National Nuclear Data Center. Nuclear Decay Data in the MIRD Format. `http://www.nndc.bnl.gov/`. Database Version of April 21, 2010.

[48] ROOT 5.26/00b. `http://root.cern.ch/`.

[49] M.J. Berger, J.H. Hubbell, S.M. Seltzer, J. Chang, J.S. Coursey, R. Sukumar, and D.S. Zucker. XCOM: Photon Cross Sections Database (version 1.3). August 2010. `http://physics.nist.gov/xcom`.

[50] A. Fasso, A. Ferrari, J. Ranft, and P.R. Sala. *FLUKA: A Multi-particle Transport Code (Program Version 2005)*. CERN, Geneva, 2005.

[51] G. Battistoni, F. Cerutti, A. Fasso, A. Ferrari, S. Muraro, J. Ranft, S. Roesler, and P. R. Sala. The FLUKA Code: Description and Benchmarking. *Hadronic Shower Simulation Workshop*, 896(1):31–49, 2007.

[52] Evelina Olofsson. Material mapping from CT-data for use in proton therapy dose calculations. Master's thesis, 2007.

[53] Florian Sommerer, Katia Parodi, Alfredo Ferrari, Karin Poljanc, Wolfgang Enghardt, and Hannes Aiginger. Investigating the accuracy of the FLUKA code for transport of therapeutic ion beams in matter. *Physics in Medicine and Biology*, 51(17):4385, 2006.

[54] J. Sempau, J. Fernandez-Varea, E. Acosta, and F. Salvat. Experimental benchmarks of the Monte Carlo code PENELOPE. *Nuclear Inst and Methods in Physics Research*, 207(2):107–203, 2003.

[55] A. Mairani, S Brons, F Cerutti, A Fasso, A Ferrari, M Kramer, K Parodi, M Scholz, and F Sommerer. The FLUKA Monte Carlo code coupled with the local effect model for biological calculations in carbon ion therapy. *Physics in Medicine and Biology*, 55(15):4273, 2010.

A Tabulated elemental compositions

Table 17: Mass densities and elemental compositions by percentage of mass for soft tissues. The values are taken from ICRU Report 44 [38] and 46 [37], Woodard and White [39] and White et al. [40].

		w_i^{el} (% by mass)										
Tissue	ρ/ [gcm^3]	H	C	N	O	Na	S	Cl	P	K	Fe	Ca
Adipose tissue 1[a]	0.97	11.2	51.7	1.3	35.5	0.1	0.1	0.1	-	-	-	-
Adipose tissue 2[a]	0.95	11.4	59.8	0.7	27.8	0.1	0.1	0.1	-	-	-	-
Adipose tissue 3[a]	0.93	11.6	68.1	0.2	19.8	0.1	0.2	0.1	-	-	-	-
Adrenal gland[a]	1.03	10.6	28.4	2.6	57.8	-	0.2	0.2	0.1	0.1	-	-
Aorta[a]	1.05	9.9	14.7	4.2	69.8	0.2	0.3	-	0.4	0.1	-	0.4
Blood - whole[a]	1.06	10.2	11.0	3.3	74.5	0.1	0.2	0.3	0.1	0.2	0.1	-
Blood - erythrocytes[a]	1.09	9.5	19.0	5.9	64.6	-	0.3	0.2	0.1	0.3	0.1	-
Blood - plasma[a]	1.03	10.8	4.1	1.1	83.2	0.3	0.1	0.4	-	-	-	-
Brain*[b]	1.04	10.7	14.5	2.2	71.2	0.2	0.2	0.3	0.4	0.3	-	-
Brain, white matter[a]	1.04	10.6	19.4	2.5	66.1	0.2	0.2	0.3	0.4	0.3	-	-
Brain, grey matter[a]	1.04	10.7	9.5	1.8	76.7	0.2	0.2	0.3	0.3	0.3	-	-
Breast†[c]	0.96	11.5	38.7	-	49.8	-	-	-	-	-	-	
Cerebrospinal fluid[a]	1.01	11.1	-	-	88.0	0.5	-	0.4	-	-	-	-
Connective tissue[a]	1.12	9.4	20.7	6.2	62.2	0.6	0.6	0.3	-	-	-	-
Eye lens[a]	1.07	9.6	19.5	5.7	64.6	0.1	0.3	0.1	0.1	-	-	-
Gallbladder bile[a]	1.03	10.8	6.1	0.1	82.2	0.4	-	0.4	-	-	-	-
GI-tract‡[a]	1.03	10.6	11.5	2.2	75.1	0.1	0.1	0.2	0.1	0.1	-	-
Heart, bloodfilled[a]	1.06	10.3	12.1	3.2	73.4	0.1	0.2	0.3	0.1	0.2	0.1	-
Heart 1[a]	1.05	10.3	17.5	3.1	68.1	0.1	0.2	0.2	0.2	0.3	-	-
Heart 2[a]	1.05	10.4	13.9	2.9	71.8	0.1	0.2	0.2	0.2	0.3	-	-
Heart 3[a]	1.05	10.4	10.3	2.7	75.6	0.1	0.2	0.2	0.2	0.3	-	-
Kidney 1[a]	1.05	10.2	16.0	3.4	69.3	0.2	0.2	0.2	0.2	0.2	-	0.1
Kidney 2[a]	1.05	10.3	13.2	3	72.4	0.2	0.2	0.2	0.2	0.2	-	0.1
Kidney 3[a]	1.05	10.4	10.6	2.7	75.2	0.2	0.2	0.2	0.2	0.2	-	0.1
Lipid[c]	0.92	11.8	77.3	-	10.9	-	-	-	-	-	-	-
Liver 1[a]	1.05	10.3	15.6	2.7	70.1	0.2	0.3	0.2	0.3	0.3	-	-
Liver 2[a]	1.06	10.2	13.9	3	71.6	0.2	0.3	0.2	0.3	0.3	-	-
Liver 3[a]	1.07	10.1	12.6	3.3	72.7	0.2	0.3	0.2	0.3	0.3	-	-

*1:1 mixture of grey and white brain matter
† 1:1 mixture of water and lipid
‡ small intestine wall
[a]Woodard and White (1986)
[b] ICRU Report 44
[c] ICRU Report 46

Table 17 cont.

		w_i^{el} (% by mass)									
Tissue	ρ/ [gcm^3]	H	C	N	O	Na	S	Cl	P	K	I
Lung - inflated [c]	0.26	10.3	10.5	3.1	74.9	0.2	0.3	0.3	0.2	0.2	-
Lung - deflated [c]	1.05	10.3	10.5	3.1	74.9	0.2	0.3	0.3	0.2	0.2	-
Lymph [c]	1.03	10.8	4.1	1.1	83.2	0.3	0.1	0.4	-	-	-
Mammary gland 1 [a]	0.99	10.9	50.6	2.3	35.8	0.1	0.1	0.1	0.1	-	-
Mammary gland 2[a]	1.02	10.6	33.2	3.0	52.8	0.1	0.2	0.1	0.1	-	-
Mammary gland 3[a]	1.06	10.2	15.8	3.7	69.8	0.1	0.2	0.1	0.1	-	-
Muscle - skeletal 1[a]	1.05	10.1	17.1	3.6	68.1	0.1	0.3	0.1	-	0.4	-
Muscle - skeletal 2[a]	1.05	10.2	14.3	3.4	71.0	0.1	0.3	0.1	-	0.4	-
Muscle - skeletal 3[a]	1.05	10.2	11.2	3.0	74.5	0.1	0.3	0.1	-	0.4	-
Ovary [a]	1.05	10.5	9.3	2.4	76.8	0.2	0.2	0.2	0.2	0.2	-
Pancreas[a]	1.04	10.6	16.9	2.2	69.4	0.2	0.1	0.2	0.2	0.2	-
Prostate[a]	1.04	10.5	8.9	2.5	77.4	0.2	0.2	-	0.1	0.2	-
Protein[c]	1.35	6.6	53.4	17.0	22.0	-	1.0	-	-	-	-
Skin 1[a]	1.09	10.0	25	4.6	59.4	0.2	0.3	0.3	0.1	0.1	-
Skin 2[a]	1.09	10.0	20.4	4.2	64.5	0.2	0.2	0.3	0.1	0.1	-
Skin 3[a]	1.09	10.1	15.8	3.7	69.5	0.2	0.2	0.3	0.1	0.1	-
"Soft tissue"[d]	1.03	10.5	25.6	2.7	60.2	0.1	0.3	0.2	0.2	0.2	-
Stomach[a]	1.05	10.4	13.9	2.9	72.1	0.1	0.2	0.1	0.1	0.2	-
Spleen[a]	1.06	10.3	11.3	3.2	74.1	0.1	0.2	0.2	0.3	0.3	-
Thyroid[a]	1.05	10.4	11.9	2.4	74.5	0.2	0.1	0.2	0.1	0.1	0.1
Trachea[a]	1.06	10.1	13.9	3.3	71.3	0.1	0.4	0.1	0.4	0.1	-
Urinary bladder - empty[a]	1.04	10.5	9.6	2.6	76.1	0.2	0.2	0.3	0.2	0.3	-
Urinary bladder - filled [a]	1.03	10.8	3.5	1.5	83	0.3	0.1	0.5	0.1	0.2	-
Water [b]	1.00	11.2	-	-	88.8	-	-	-	-	-	-

[a] Woodard and White (1986)
[b] ICRU Report 44
[c] ICRU Report 46
[d] White et al. (1987)

Table 18: Mass densities and elemental compositions by percentage of mass for skeletal tissues. The values were taken from ICRU Report 46 [37], Woodard and White [39] and White et al. [40].

		w_i^{el} (% by mass)											
Tissue	$\frac{\rho}{[\mathrm{gcm}^3]}$	H	C	N	O	Na	S	Cl	P	K	Fe	Ca	Mg
Cartilage[a]	1.10	9.6	9.9	2.2	74.4	0.5	0.9	0.3	2.2	-	-	-	-
Cortical bone[a]	1.92	3.4	15.5	4.2	43.5	0.1	0.3	-	10.3	-	-	22.5	0.2
Cranium [d]	1.61	5.0	21.2	4.0	43.5	0.1	0.3	-	8.1	-	-	17.6	0.2
Femur (30 y.) [c]	1.33	7.0	34.5	2.8	36.8	0.1	0.2	0.1	5.5	-	-	12.9	0.1
Femur (90 y.)[c]	1.22	7.9	38.5	2.2	36.2	0.1	0.1	0.1	4.4	-	-	10.4	0.1
Femur - total bone [d]	1.42	6.3	33.3	2.9	36.2	0.1	0.2	-	6.6	-	-	14.3	0.1
Humerus - total bone[d]	1.46	6.0	31.4	3.1	36.9	0.1	0.2	-	7.0	-	-	15.2	0.1
Mandible [d]	1.68	4.6	19.9	4.1	43.5	0.1	0.3	-	8.6	-	-	18.7	0.2
Ribs (2nd. 6th) [d]	1.41	6.4	26.3	3.9	43.6	0.1	0.3	0.1	6.0	0.1	-	13.1	0.1
Ribs (10th) [d]	1.52	5.6	23.5	4.0	43.4	0.1	0.3	0.1	7.2	0.1	-	15.6	0.1
Yellow marrow[a]	0.98	11.5	64.4	0.7	23.1	0.1	0.1	0.1	-	-	-	-	-
Red marrow[a]	1.03	10.5	41.4	3.4	43.9	-	0.2	0.2	0.1	0.2	0.1	-	-
Spongiosa *[a]	1.18	8.5	40.4	2.8	36.7	0.1	0.2	0.2	3.4	0.1	0.1	7.4	0.1
Vert. col.(C4)† [d]	1.42	6.3	26.1	3.9	43.6	0.1	0.3	0.1	6.1	0.1	-	13.3	0.1
Vert. col.(D6. L3) [d]	1.33	7.0	28.7	3.8	43.7	-	0.2	0.1	5.1	0.1	0.1	11.1	0.1
Vert. col. - whole[d]	1.33	7.1	25.8	3.6	47.2	0.1	0.3	0.1	5.1	0.1	-	10.5	0.1
Sternum[d]	1.25	7.8	31.6	3.7	43.8	-	0.2	0.1	4.0	0.1	0.1	8.5	0.1
Clavicle, scapula[d]	1.46	6.0	31.3	3.1	37.0	0.1	0.2	-	7.0	-	-	15.2	0.1
Innominate male [d]	1.41	6.3	26.2	3.9	43.6	0.1	0.3	0.1	6.1	0.1	-	13.2	0.1
Innominate female[d]	1.46	6.0	25	3.9	43.5	0.1	0.3	0.1	6.6	0.1	0.1	14.3	-
Sacrum male[d]	1.29	7.4	30.2	3.7	43.8	-	0.2	0.1	4.5	0.1	0.1	9.8	0.1
Sacrum female[d]	1.39	6.6	27.1	3.8	43.5	0.1	0.3	0.1	5.8	0.1	-	12.5	0.1

* 1/3 cortical bone, 1/3 yellow marrow, 1/3 red marrow
† excluding cartilage

[a] Woodard and White (1986)
[c] ICRU Report 46
[d] White et al. (1987)

B MATLAB script for extracting mass fractions

The vector notation presented in Section 3.1 is useful to introduce the graphical interpretation of the decomposition algorithms, but when extracting base material mass fractions for a large number of tissues it may be more suitable with a matrix notation.

The mass density assumption that was introduced for the 3MDv method (Eq. 33) requires that the volume of each component is preserved in the mixture. This implies that volume fractions of base materials can be converted to mass fractions without any loss of information. This relationship is used in the following treatment where the 3MDv method is presented in a matrix notation.

As shown in Section 3.1.3, the μ-values at two photon energies, E_1 and E_2, of a mixture of three base materials can be be expressed as:

$$\begin{aligned}\mu(E_1) &= v_1\mu_1(E_1) + v_2\mu_2(E_1) + v_3\mu_3(E_1)\\ \mu(E_2) &= v_1\mu_1(E_2) + v_2\mu_2(E_2) + v_3\mu_3(E_2)\\ 1 &= v_1 + v_2 + v_3\end{aligned}$$

Where the third equation follows from the assumption that the three base material volumes adds up to the volume of the mixture.

This system of equations can be written in a matrix notation as:

$$\underbrace{\begin{bmatrix}\mu_1(E_1) & \mu_2(E_1) & \mu_3(E_1)\\ \mu_1(E_1) & \mu_2(E_1) & \mu_3(E_1)\\ 1 & 1 & 1\end{bmatrix}}_{A}\underbrace{\begin{bmatrix}v_1\\ v_2\\ v_3\end{bmatrix}}_{v} = \underbrace{\begin{bmatrix}\mu(E_1)\\ \mu(E_2)\\ 1\end{bmatrix}}_{b} \tag{49}$$

The volume fractions may then be extracted by e.g. finding the inverse matrix of b:

$$v = Ab^{-1} \tag{50}$$

When the volumes of the base materials are preserved in the mixture, it is analogous to describe the base material proportions by masses or by volumes. As long as the mass densities are known, conversion can be done between v and m without loss of information. The conversion can be done using the mass densities of the base materials (ρ_i) and the tissue (ρ):

$$w_i = \frac{m_i}{m} = \frac{V_i}{V}\frac{\rho_i}{\rho} = v_i\frac{\rho_i}{\rho} \tag{51}$$

In matrix notation, the conversion from volume fractions to mass fractions can be performed as:

$$\underbrace{\begin{bmatrix} w_1^1 & w_1^2 & w_1^3 & \dots \\ w_2^1 & w_2^2 & w_2^3 & \dots \\ w_3^1 & w_3^2 & w_3^3 & \dots \end{bmatrix}}_{w_{base}^{tissue}} = \underbrace{\begin{bmatrix} \rho_1 & 0 & 0 \\ 0 & \rho_2 & 0 \\ 0 & 0 & \rho_3 \end{bmatrix}}_{\rho_{base}} \underbrace{\begin{bmatrix} v_1^1 & v_1^2 & v_1^3 & \dots \\ v_2^1 & v_2^2 & v_2^3 & \dots \\ v_3^1 & v_3^2 & v_3^3 & \dots \end{bmatrix}}_{v_{base}^{tissue}} \underbrace{\begin{bmatrix} 1/\rho^1 & 0 & 0 & \dots \\ 0 & 1/\rho^2 & 0 & \dots \\ 0 & 0 & 1/\rho^3 & \dots \\ \vdots & \vdots & \vdots & \ddots \end{bmatrix}}_{\rho^{tissue}} \tag{52}$$

where ρ_{base} contains the mass densities of the base materials and ρ^{tissue} the mass densities of each tissue for which the proportions are to be extracted.

The following MATLAB script uses the matrix solution to extract elemental compositions.

```
clear all

%%% Preparation of data %%%

% mass attenuation coefficients for all spectra:

[M80,M100,M120,M140,M140Sn,Names] =...
    textread('MacsOfTissues.txt','%f␣%f␣%f␣%f␣%f␣%s');

% linear attenuation coefficients for all spectra:

[L80,L100,L120,L140,L140Sn,LNames] =...
    textread('LacsOfTissues.txt','%f␣%f␣%f␣%f␣%f␣%s');

% D (79x1) - densities for all tissues:

[DNames, D] = textread('list_of_densities.txt', '%s␣%f');

% M (5x79) - mass attenuation coefficients for all tissues
% at mean energies of different spectra:

M(:,1) = M80;
M(:,2) = M100;
M(:,3) = M120;
M(:,4) = M140;
M(:,5) = M140Sn;

% L (5x79) - linear attenuation coefficients for all tissues
% at mean energies of different spectra:

L(:,1) = L80;
L(:,2) = L100;
L(:,3) = L120;
```

```
L(:,4) = L140;
L(:,5) = L140Sn;

%selection of two spectra:

spek1 = 1;
spek2 = 5;
c1 = 79; %base material 1 - (water)
c2 = 28; %base material 2 - (lipid)
c3 = 45; %base material 3 - (protein)


% b (79x3) - linear attenuation coefficients for all tissues
% at the mean energies of the spectra considered
%          Adi1 Adi2 Adi3 Pro..
%u(le)
%u(he)
%c(1,1,1)

for i = 1:length(L);
b(i,:) = [L(i,spek1); L(i,spek2); 1];
end


% A (3x3) - linear attenuation coefficients for base materials
% at the mean energies of the spectra considered
%          wat lip pro
%u(le)
%u(he)
%c(1,1,1)

A = [L(c1,spek1), L(c2,spek1), L(c3,spek1);...
    L(c1,spek2), L(c2,spek2), L(c3,spek2);...
    1, 1, 1];

%v - volume fractions (3x79):
%        adi1 adi2 adi3..
% wat
% lip
% pro

v = A\b';
```

```
    %%% Volume fractions to mass fractions %%%
%%% (mass fractions with volume preservation) %%%

%d_i (3x3): diagnonal matrix with mass density of base materials
d_i = eye(3);
d_i(1,:) = d_i(1,:) * D(c1);
d_i(2,:) = d_i(2,:) * D(c2);
d_i(3,:) = d_i(3,:) * D(c3);

% d_v (79x1): reciprocal densities for all tissues
% under volume preservation assumption
for i = 1:length(L)
    d_v(:,i) = 1 / ( v(1,i)*D(c1)+v(2,i)*D(c2)+v(3,i)*D(c3) );
end
% (79x1) -> (1x79)
d_v = d_v';

%diagonal matrix with reciprocal values of
% mass densities for classified tissues

d_t = eye(79);
for i=1:length(L)
    d_t(:,i) = d_t(:,i) * d_v(i);
end

% w_v - mass fractions with volume preservation (3x79)
% w_v = v_1 * dens_1 * 1/dens_tot

w_temp = v' * d_i;
w_v = w_temp' * d_t;


%%% Mass fractions without volume preservation %%%

% b_t (3x79) - mass attenuation coefficients for all tissues:
%           Adi1 Adi2 Adi3..
%u/rho(le)
%u/rho(he)
%c(1,1,1)

for i=1:length(M)
    b_t(:,i) = [M(i,spek1); M(i,spek2); 1];
end

% A_t (3x3) - mass attenuation coefficients for base materials:
```

```
%           wat lip pro
%u/rho(le)
%u/rho(he)
%c(1,1,1)

A_t =[M(c1,spek1), M(c2,spek1), M(c3,spek1);...
    M(c1,spek2), M(c2,spek2), M(c3,spek2);...
    1, 1, 1];

% w_t (3x79) - weight fractions without volume preservation:

w_t = A_t\b_t;

%%% Extraction of elemental mass fractions %%%

% ec (13x79) - tabulated elemental weights for all tissues:

[N,rho,h,c,n,o,na,s,cl,p,k,fe,ca,mg,i] =...
    textread('at_comp.csv',...
    '%s␣%f␣%f␣%f␣%f␣%f␣%f␣%f␣%f␣%f␣%f␣%f␣%f␣%f␣%f',...
    'delimiter',';','headerlines',1);

ec = [h, c, n ,o, na, s, cl, p, k, fe, ca, mg, i];
ec = ec*0.01;

% base_ec (3x13) - elemental composition of base materials:

base_ec(1,:) = ec(c1,:);
base_ec(2,:) = ec(c2,:);
base_ec(3,:) = ec(c3,:);

% el_v (13x79) - classified elemental compositions
%with volume preservation

el_v = base_ec' * w_v;

% el_t (13x79) - classified elemental compositions
%without volume preservation

el_t = base_ec' * w_t;
```

C PENELOPE input file for ^{192}Ir simulations

```
TITLE  Energy imparted to water. Ir-192.
       .
       >>>>>>>> Input phase-space file (psf).
IPSFN  penPsf.txt          [Input psf name, up to 20 characters]
IPSPLI 10
EPMAX  8.85e5
       .
       >>>>>>>> Material data and simulation parameters.
MFNAME water.mat                       [Material file, up to 20 chars]
MSIMPA 1.0e5 1.0e3 1.0e4 0.1 0.1 1e4 1e3    [EABS(1:3),C1,C2,WCC,WCR]
MFNAME water.mat
MSIMPA 1.0e6 1.0e4 1.0e4 0.1 0.1 1e6 1e4    [EABS(1:3),C1,C2,WCC,WCR]
       .
       >>>>>>>> Geometry definition file.
GEOMFN spheres.geo                     [Geometry file, up to 20 chars]
       .
       >>>>>>>> Dose distribution.
GRIDX  -3.125,3.125
GRIDY  -3.125,3.125
GRIDZ  -2.375,2.375
GRIDBN 25,25,19           [Energy window and number of channels]
       .
       >>>>>>>> Job properties
RESUME dump.dmp                [Resume from this dump file, 20 chars]
DUMPTO dump.dmp                  [Generate this dump file, 20 chars]
DUMPP  60                                  [Dumping period, in sec]
       .
NSIMSH 5e25
TIME   3.6e5                        [Allotted simulation time, in sec]
       .
END                                  [Ends the reading of input data]
```

D MATLAB script for creating dose volume histograms

```
clear all

%%%%%%%%%%%% Preparation of data %%%%%%%%%%%%

% input of x,y,z coordinates and corresponding absorbed dose
[dose1(:,1),dose1(:,2),dose1(:,3),dose1(:,4)] =...
    textread('case1_3d-dose.dat','%f␣%f␣%f␣%f␣%*n␣%*n␣%*n␣%*n','...
    'headerlines',12);

% input of PTV mask
[b] = textread('data_PTV4_map.txt','%n');

% dimensions of scoring volume
nx = 25;
ny = 25;
nz = 6;

% change dimension of PTV mask
ptv = reshape(b,nx,ny,nz);

% rotates the masks to match scoring grid
for j=1:6;
    ptv(:,:,j) = rot90(ptv(:,:,j),3);
end

% prepare space
temp_ptv=zeros(25,25,19);

% ptv is expanded from 25x25x6 to
% 25x25x19 to match scoring grid
for i=1:3
    temp_ptv(:,:,i) = ptv(:,:,1);
end
for i=4:6
    temp_ptv(:,:,i) = ptv(:,:,2);
end
for i=7:9
    temp_ptv(:,:,i) = ptv(:,:,3);
end
for i=10:12
    temp_ptv(:,:,i) = ptv(:,:,4);
end
for i=13:15
```

```
    temp_ptv(:,:,i) = ptv(:,:,5);
end
for i=16:19
    temp_ptv(:,:,i)=ptv(:,:,6);
end
ptv=temp_ptv;


% geometrical limits for the scoring grid
xmin = min(dose1(:,1));
xmax = max(dose1(:,1));
ymin = min(dose1(:,2));
ymax = max(dose1(:,2));
zmin = min(dose1(:,3));
zmax = max(dose1(:,3));

% resolution of the scoring grid
xres=25;
yres=25;
zres=19;

% linspace defines a vector representing
% the ranges of the x- and y-dimensions

xv = linspace(xmin,xmax,xres);
yv = linspace(ymin,ymax,yres);
zv = linspace(zmin,zmax,zres);

% reshape the scoring grid from 11875x4 to 25x25x19
% meshgrid calculates the grid matrix
% for the x- y- and z-coordinates

[xi,yi,zi] = meshgrid(xv,yv,zv);

% assign dose to the X-Y-Z 25x25x19 scoring grid

w = griddata3(dose1(:,1),dose1(:,2),dose1(:,3),dose(:,4),xi,yi,zi);

%%%%%%%%%%%%% DVH %%%%%%%%%%%%%

% PTV voxels are sorted out
ptv1_dose = ptv .* w;


% reshape for histogram
```

```
for i = 1:antal;
    eval(['ptv' num2str(i) '_dose=reshape(ptv' num2str(i)...
        '_dose,11875,1);']) ;
end

% sort out non-zero elements

ind_ptv1 = find(ptv1_dose);

% hist gives histogram dor dose values
r = hist(ptv1_dose, max(ptv1_dose));


% create cumulative dvh

    for i = 1:length(r);
        dvh_ptv1(i)=sum(r(i:length(r)));
    end
```

E PENELOPE input file for ^{125}I simulations

```
TITLE  Energy imparted to prostate.
       .
       >>>>>>>> Source definition.
SKPAR  2        [Primary particles: 1=electron, 2=photon, 3=positron]

SPECTR 3.549e4 6.68e0        [E bin: lower-end and total probability]
SPECTR 3.549e4 1.00e-35      [E bin: lower-end and total probability]
SPECTR 2.747e4  7.44e1       [E bin: lower-end and total probability]
SPECTR 2.747e4  1.00e-35     [E bin: lower-end and total probability]
SPECTR 2.72e4  4.00e1        [E bin: lower-end and total probability]
SPECTR 2.72e4  1.00e-35      [E bin: lower-end and total probability]
SPECTR 3.10e4  2.60e1        [E bin: lower-end and total probability]
SPECTR 3.10e4  1.00e-35      [E bin: lower-end and total probability]
SPECTR 3.77e3  1.49e1        [E bin: lower-end and total probability]
SPECTR 3.77e3 -1.00e0        [E bin: lower-end and total probability]
SPOSIT 0 0 0                              [Coordinates of the source]
SCONE  0 0 180                          [Conical beam; angles in deg]
       .
       >>>>>>>> Material data and simulation parameters.
MFNAME water.mat                       [Material file, up to 20 chars]
MSIMPA 1.0e4 1.0e3 1.0e4 0.1 0.1 1e4 1e3    [EABS(1:3),C1,C2,WCC,WCR]
       .
       >>>>>>>> Geometry definition file.
GEOMFN spheres.geo                     [Geometry file, up to 20 chars]
       .
       >>>>>>>> Job properties
RESUME dump.dmp                [Resume from this dump file, 20 chars]
DUMPTO dump.dmp                   [Generate this dump file, 20 chars]
DUMPP  60                                      [Dumping period, in sec]
       .
NSIMSH 5e25                     [Desired number of simulated showers]
TIME   36000                       [Allotted simulation time, in sec]
       .
END                                   [Ends the reading of input data]
```

F FLUKA input file

Example of input file for FLUKA concerning a 135 MeV proton beam incident from the side.

```
TITLE
Spatial distribution of absorbed dose for a proton beam. Tabulated tissues.
RANDOMIZ          1.          1.
DEFAULTS                                                              HADROTHE
BEAM             -.135        0.0         0.0         0.0         0.0-1.0PROTON
HI-PROPE          6.          12.
EVENTYPE                                  2.                          DPMJET
PHYSICS           3.0                                                 EVAPORAT
PHYSICS           1.0                                                 COALESCE
BEAMPOS           0.0         0.0       0.001         0.0         0.0
GEOBEGIN                                                              COMBNAME
    0    0
SPH BLK           0.0  0.0  0.0  10000.0
ZCC cyl1          0.0  0.0  100.0
XYP Z1            0.0
XYP Z2            6.2
XYP Z3            10.2
XYP Z4            15.7
XYP Z5            19.5
XYP Z6            30.
END
BLKHOLE       5 +BLK +Z1 | +BLK -Z6 | +BLK -cyl1
R_ADI         5 +cyl1 -Z1 +Z2
R_SOFT        5 +cyl1 -Z2 +Z3
R_PROS        5 +cyl1 -Z3 +Z4
R_GI          5 +cyl1 -Z4 +Z5
R_SOFT2       5 +cyl1 -Z5 +Z6
END
GEOEND
MATERIAL          16.                 2.07                              SULFUR
MATERIAL          17.             0.003214                              CHLORINE
MATERIAL          15.                 1.82                              PHOSPHO
MATERIAL          19.                0.862                              POTASSIU
MATERIAL                             0.95                               ADI2
MATERIAL                             1.03                               SOFT
MATERIAL                             1.04                               PROS
MATERIAL                            1.029                               GI-T
* ICRU46. SMALL INTESTINE.
COMPOUND      -0.106  HYDROGEN     -0.115    CARBON      -.022  NITROGENGI-T
COMPOUND      -0.751    OXYGEN     -0.001    SODIUM    -0.001   PHOSPHOGI-T
COMPOUND      -0.001    SULFUR     -0.002  CHLORINE    -0.001  POTASSIUGI-T
* WW-86
COMPOUND      -0.105  HYDROGEN      -.089    CARBON      -.025  NITROGENPROS
COMPOUND       -.774    OXYGEN     -0.002    SODIUM    -0.001   PHOSPHOPROS
COMPOUND      -0.002    SULFUR     -0.002  POTASSIU                  PROS
* SOFT (MALE) WW-87
COMPOUND      -0.105  HYDROGEN      -.256    CARBON      -.027  NITROGENSOFT
COMPOUND       -.602    OXYGEN     -0.001    SODIUM    -0.002   PHOSPHOSOFT
COMPOUND       -.003    SULFUR     -0.002  CHLORINE    -0.002  POTASSIUSOFT
* ADI2. WW-86
COMPOUND      -0.114  HYDROGEN      -.598    CARBON      -.007  NITROGENADI2
COMPOUND       -.355    OXYGEN     -0.001    SULFUR    -0.001   SODIUMADI2
COMPOUND      -0.001  CHLORINE                                        ADI2
ASSIGNMA    BLCKHOLE   BLKHOLE
ASSIGNMA        ADI2     R_ADI
ASSIGNMA        SOFT     R_SOFT
```

```
ASSIGNMA          PROS      R_PROS
ASSIGNMA          GI-T        R_GI
ASSIGNMA          SOFT     R_SOFT2
USRBIN             11.       DOSE      -40.     100.0       0.0      30.0Dose
USRBIN             0.0        0.0       0.0       50.        1.       150.&
USRBIN             11.       DOSE      -41.     100.0       0.0      15.7Dose_P
USRBIN             0.0        0.0      10.2        1.        1.       550.&
RESNUCLE           3.        -39.                             R_PROS      activ
START         1000000.                                          0.0   28800.
STOP
```